On the Origins of Extreme Velocity Stars as Revealed by Large-scale Galactic Surveys

Qing-Zheng Li, Yang Huang, Xiao-Bo Dong, Hua-Wei Zhang, Timothy C. Beers, Zhen Yuan

The Astronomical Journal, 166:12 (21pp), 2023 July https://doi.org/10.3847/1538-3881/acd1dc

On the Origins of Extreme Velocity Stars as Revealed by Large-scale Galactic Surveys

Qing-Zheng Li[1,2], Yang Huang[2,3,8], Xiao-Bo Dong[1,8], Hua-Wei Zhang[4,5], Timothy C. Beers[6], and Zhen Yuan[7]
[1] Yunnan Observatories, Chinese Academy of Sciences, Kunming, Yunnan 650011, People's Republic of China; xbdong@ynao.ac.cn
[2] School of Astronomy and Space Science, University of Chinese Academy of Sciences, Beijing 100049, People's Republic of China; huangyang@ucas.ac.cn
[3] Key Laboratory of Space Astronomy and Technology, National Astronomical Observatories, Chinese Academy of Sciences, Beijing 100101, People's Republic of China
[4] Department of Astronomy, School of Physics, Peking University, Beijing 100871, People's Republic of China
[5] Kavli Institute for Astronomy and Astrophysics, Peking University, Beijing 100871, People's Republic of China
[6] Department of Physics and Astronomy and JINA Center for the Evolution of the Elements (JINA-CEE), University of Notre Dame, Notre Dame, IN 46556, USA
[7] Université de Strasbourg, CNRS, Observatoire Astronomique de Strasbourg, UMR 7550, F-67000 Strasbourg, France
Received 2022 July 10; revised 2023 April 27; accepted 2023 April 27; published 2023 June 12

Abstract

We assemble a large sample of 12,784 high-velocity stars with total velocity $V_{GSR} \geqslant 300\,km\,s^{-1}$, selected from RAVE DR5, SDSS DR12, LAMOST DR8, APOGEE DR16, GALAH DR2, and Gaia EDR3. In this sample, 52 are marginally hypervelocity star (HVS) candidates that have V_{GSR} exceeding their local escape velocities within 2σ confidence levels, 40 of which are discovered for the first time. All of the candidates are metal-poor, late-type halo stars, which are significantly different from the previously identified HVSs, which are largely massive early-type stars, discovered by extreme radial velocity. This finding suggests that our newly identified HVS candidates are ejected by different mechanisms from the previous population. To investigate their origins, for 547 extreme velocity stars with $V_{GSR} \geqslant 0.8V_{esc}$, we reconstruct their backward-integrated trajectories in the Galactic potential. According to the orbital analysis, no candidates are found to be definitely ejected from the Galactic-center (GC), while eight metal-poor extreme velocity stars are found to have a closest distance to the GC within 1 kpc. Intriguingly, 15 extreme velocity stars (including 2 HVS candidates) are found to have experienced close encounters with the Sagittarius dSph, suggesting that they originated from this dSph. This hypothesis is supported by an analysis of the [α/Fe]–[Fe/H] diagram. From a preliminary analysis of all of the 547 extreme velocity stars, we propose a general picture–star ejection from Galactic subsystems such as dwarf galaxies and globular clusters can be an important channel to produce extreme velocity stars or even HVSs, particularly the metal-poor late-type halo population.

Unified Astronomy Thesaurus concepts: Hypervelocity stars (776); Black holes (162); Sagittarius dwarf spheroidal galaxy (1423); Galaxy kinematics (602); Galaxy dynamics (591)

Supporting material: machine-readable tables

1. Introduction

The majority of stars in our Galaxy either rotate around the Galactic center (GC) with a typical velocity of 200–240 $km\,s^{-1}$ (e.g., Bovy et al. 2012; Huang et al. 2016; Eilers et al. 2019) in the disk region or exhibit large random motions of 100–150 $km\,s^{-1}$ in the halo (Xue et al. 2008; Huang et al. 2016). However, over the past decade, spectroscopic observations from large-scale Galactic surveys such as the Sloan Extension for Galactic Understanding and Exploration (SEGUE, Yanny et al. 2009; SEGUE-2, Rockosi et al. 2022), the LAMOST Galactic surveys (Deng et al. 2012; Zhao et al. 2012; Liu et al. 2014), and the Gaia mission (Gaia Collaboration et al. 2016) have demonstrated the existence of high-velocity stars (HiVels) in our Galaxy, some of which are even hypervelocity stars (HVSs), with total Galactocentric velocities, V_{GSR}, exceeding their local escape speeds, V_{esc}. The discoveries of such rare objects provide an important tool to explore the mass distribution of the Milky Way, especially its dark component (e.g., Gnedin et al. 2005; Rossi et al. 2017; Contigiani et al. 2019).

Over the past few decades, several ejection mechanisms have been proposed to explain the presence of HiVels/HVSs in the Milky Way, as briefly summarized below:

Black hole ejection (BHE): The so-called HVSs (with velocities even greater than 1000 $km\,s^{-1}$) were first predicted from the theoretical arguments of Hills (1988), and attributed to be the result of tidal interaction between a close stellar binary system and a supermassive black hole (SMBH) in the GC, commonly referred to as the "Hills mechanism." HVSs/HiVels can also be ejected by extending the Hills mechanism with alternative assumptions: (1) a SMBH binary or the pair of a SMBH and an intermediate-mass black hole (IMBH) in the GC (e.g., Yu & Tremaine 2003; Gualandris & Merritt 2009; Rasskazov et al. 2019), or (2) individual IMBHs (or SMBHs) in the Galactic dwarf galaxies or globular clusters, or even massive BH binaries in such Galactic subsystems (e.g., Boubert & Evans 2016; Fragione & Gualandris 2019).

Supernova explosion (SNE) in binary systems: Both core-collapse and thermonuclear supernova (SN) explosions in binary systems can disrupt the system and kick their companion stars sufficiently for them to become HiVels/HVSs (e.g., Blaauw 1961; Portegies Zwart 2000; Hansen 2003; Justham et al. 2009; Wang & Han 2009; Pakmor et al. 2013; Zubovas et al. 2013; Shen et al. 2018; Bauer et al. 2019; Neunteufel 2020). Typically, the core-collapse SN explosions cannot eject stars with very high velocity (no greater than 300–400 $km\,s^{-1}$; Portegies Zwart 2000). This mechanism is

[8] Corresponding authors.

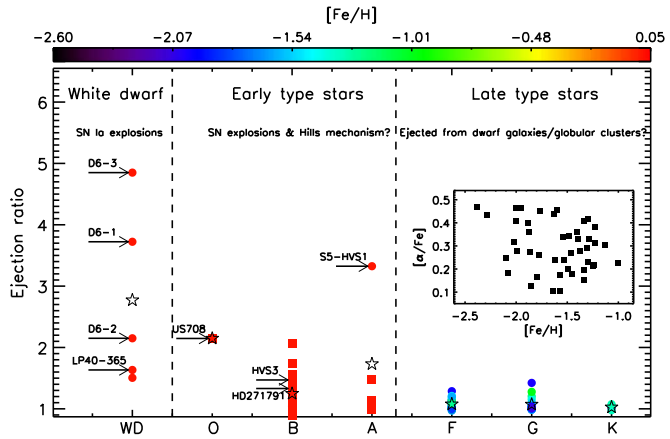

Figure 1. Ejection ratios for 88 HVSs and candidates from the literature and the current work, as a function of spectral type, color-coded by metallicity. Here we adopt the escape velocity curve from Williams et al. (2017) to calculate the ejection ratio. As mentioned in Section 3.3, the 52 late-type stars found in this work are mariginally HVS candidates given their large velocity uncertainties. The ejection ratio is defined to be the ratio of the total or radial velocity in the Galactic rest frame to the local escape velocity of a star. Note that the [Fe/H] values for white dwarf and early-type stars are assumed to be Solar ([Fe/H] = zero). The open asterisk marks the average ejection ratio of the corresponding spectral type. The inset shows the chemical distribution of the late-type stars discovered in the current work in the [α/Fe]–[Fe/H] plane.

mainly used to account for the existence of OB runaway stars above the Galactic plane (Blaauw 1961). HVSs with velocities above 1000 km s^{-1} can be ejected in thermonuclear SN explosions, with progenitors of either white dwarf (WD)–WD binaries (e.g., Shen et al. 2018) or binaries comprising a WD plus a non-degenerate star (e.g., Han 2008; Wang & Han 2009; Bauer et al. 2019; Neunteufel 2020).

Dynamical ejection mechanism (DEM): This was an alternative theory to explain the Galactic OB runaway stars, which was first proposed by Poveda et al. (1967). In this mechanism, runaway stars are ejected as a consequence of close stellar encounters in young stellar clusters. The typical maximum kick velocity achieved by this mechanism is around 300–400 km s^{-1}, resulting from collisions between two close binaries (e.g., Leonard & Duncan 1990; Leonard 1991; Gvaramadze et al. 2009).

Tidal stripping from dwarf galaxies (TSD): According to this theory, stars can be stripped with high velocity from a dwarf galaxy being tidally disrupted by the gravity field of the Milky Way (MW) during its pericentric passage (Abadi et al. 2009). In this mechanism, a massive dwarf galaxy ($>10^{10}$ $M_{\odot}$) is required to eject unbound stars (Piffl et al. 2011).

Observationally, the first HVS, a B-type star with an extreme radial velocity of 709 km s^{-1} in the Galactic rest frame, was discovered by Brown et al. (2005). After that, over two dozen HVSs, all being early-type, were either serendipitous discoveries (Hirsch et al. 2005; Heber et al. 2008; Koposov et al. 2020), or resulted from dedicated follow-up surveys (Brown et al. 2006, 2007, 2009, 2012, 2014; Zheng et al. 2014; Huang et al. 2017; Li et al. 2018). The only low-mass HVS among these early-type stars is US 708, an O-type subdwarf compact helium star with a total velocity of around 994 km s^{-1} (Hirsch et al. 2005; Geier et al. 2015; Neunteufel 2020, see Figure 1), which was suggested to be ejected from a SN Ia explosion (Geier et al. 2015). The remaining HVSs are young, massive B/A-type stars, and are mostly identified from their extreme radial velocities only. Among them, HVS3 (or HE 0437-5439) was suggested to have been ejected from the Large Magellanic Cloud (LMC) via the Hills mechanism (Edelmann et al. 2005), which was confirmed by the Gaia data (Irrgang et al. 2018; Erkal et al. 2019). HD 271791 was suggested to have been ejected from the Galactic disk, either via DEM (Gvaramadze et al. 2009) or SNE (Przybilla et al. 2008). Recently, S5-HVS1, an A-type star with a total velocity of 1755 ± 50 km s^{-1}, was discovered to point unambiguously to the GC, based on its backward-integrated trajectory (Koposov et al. 2020), providing solid evidence of the operation of the Hills mechanism in our Galaxy. We note that previous efforts have searched for late-type HVSs (Li et al. 2012, 2015; Palladino et al. 2014), but almost all of these are likely bound to our Galaxy, with a single exception (LAMOSTJ115209.12+120258.0), as revisited by Ziegerer et al. (2015) or Boubert et al. (2018). Figure 1 shows the ejection ratio (defined as the ratio between the total or radial velocity in the Galactic rest frame and the local escape velocity), as a function of spectral type, for the known HVSs and candidates (including those found in the current work).

Thanks to the Gaia mission (Gaia Collaboration et al. 2018, 2021), several dozen new HVSs and candidates have been discovered, using very precise astrometric parameters (e.g., Bromley et al. 2018; Du et al. 2018, 2019; Shen et al. 2018; Irrgang et al. 2019; Marchetti et al. 2019; Marchetti 2021; Li et al. 2020). Among those sources, Shen et al. (2018) found three hypervelocity WDs. These three WDs, together with LP 40-365 and three other potential high-velocity WDs (Vennes et al. 2017; Raddi et al. 2018, 2019), provide direct evidence for the operation of the SNE ejection mechanism in the Galaxy (especially the dynamically driven double-degenerate double-detonation–D6 channel; Shen et al. 2018). Astrometry from Gaia has also enabled more precise measurements of 3D velocities for those known massive B/A-type HVSs, which further improves our understanding of their origins (Hattori et al. 2019; Kreuzer et al. 2020; Irrgang et al. 2021).

In this paper, we present the results of a new systematic search for HiVels from the combination of astrometric data from the Gaia early data release 3 (EDR3) and large-scale spectroscopic surveys, including the RAVE DR5, SDSS DR12, LAMOST DR8, APOGEE DR16, and GALAH DR2 surveys. A sample of 12,784 HiVels (including 6966 halo stars and 5818 disk stars) with total velocities $V_{\rm GSR} \geqslant 300$ km s^{-1} are found. Interestingly, 52 of them are HVS candidates but with total velocities marginally exceeding the local escape velocities (see Figure 1). All of these candidates are late-type metal-poor stars, which are significantly different from those HVSs in the literature (primarily massive early-type stars) that were mostly found by their extreme radial velocities alone (see Figure 1). Our newly discovered late-type HVS candidates, together with the known ones, shed additional light on their likely ejection mechanisms.

This paper is organized as follows. In Section 2, we briefly introduce the data we employ. In Sections 3 and 4, we present the main results and compare them with previous studies. We discuss the origins of the newly discovered extreme velocity stars with $V_{\rm GSR} \geqslant 0.8 V_{\rm esc}$ in Section 5. Finally, a summary is presented in Section 6.

2. Data

In the current work, we use data from modern large-scale Galactic spectroscopic surveys, including the RAVE (Steinmetz et al. 2006), SDSS (Alam et al. 2015), LAMOST (Deng et al. 2012; Liu et al. 2014), APOGEE (Majewski et al. 2017) and GALAH (De Silva et al. 2015) surveys, as well as from the Gaia astrometric survey (Gaia Collaboration et al. 2016, 2018, 2021).

2.1. Spectroscopic Surveys

After nearly 10 years of effort (2003–2013), the RAVE survey (Steinmetz et al. 2006) collected 520,781 moderate-resolution ($R\sim7500$) spectra centered on the Ca I triplet (8410–8795 Å) for 457,588 unique stars, randomly selected from stars in the Southern Hemisphere with $9<I<12$, using the multi-object spectrograph 6dF on the 1.2 m UK Schmidt Telescope of the Australian Astronomical Observatory. Estimates of line-of-sight velocities, stellar atmospheric parameters (effective temperature, $T_{\rm eff}$, surface gravity, $\log g$, and metallicity, [Fe/H]), as well as α-element abundances for RAVE DR5 stars are described in Kunder et al. (2017). The typical uncertainties are 2 km s^{-1}, 250 K, 0.4 dex, 0.2 dex, and 0.2 dex for $v_{\rm los}$, $T_{\rm eff}$, $\log g$, [Fe/H], and [α/Fe], respectively.

In this study, we also consider the data for over 800,000 stellar spectra (for over 700,000 stars) from SDSS DR12 (Alam et al. 2015), collected by the main SDSS survey, SEGUE (Yanny et al. 2009), SEGUE-2 (Rockosi et al. 2022), and the Baryon Oscillation Spectroscopic Survey (BOSS; Dawson et al. 2013). The $v_{\rm los}$, stellar atmospheric parameters, and [α/Fe] abundance ratios are obtained from those spectra with the SEGUE Stellar Parameter Pipeline (SSPP; Lee et al. 2008a, 2011). Typical uncertainties are 5–10 km s^{-1}, 130 K, 0.21 dex, 0.11 dex, and 0.10 dex for $v_{\rm los}$, $T_{\rm eff}$, $\log g$, [Fe/H], and [α/Fe], respectively (Allende Prieto et al. 2008; Lee et al. 2008b; Smolinski et al. 2011).

LAMOST is a 4 m quasi-meridian reflecting Schmidt telescope that is equipped with 4000 fibers distributed over a field of view that is 5° in diameter (Cui et al. 2012). It can collect 4000 optical spectra per exposure, with wavelength coverage ranging from 3700 to 9000 Å, and spectral resolving power around $R=2000$. In the current work, we adopt the data from LAMOST DR8,[9] which has released 6.5 million stellar spectra with reliable stellar parameter measurements for about four million unique stars. The $v_{\rm los}$ and stellar atmospheric parameters and from LAMOST spectra are derived by the official pipeline, i.e., the LAMOST Stellar Parameter Pipeline (LASP; Luo et al. 2015). The typical uncertainties achieved by this pipeline are 5 km s^{-1}, 100 K, 0.25 dex, and 0.10 dex for $v_{\rm los}$, $T_{\rm eff}$, $\log g$, and [Fe/H], respectively. In addition to the parameters from the official pipeline, we also adopt the values of [α/Fe] determined by Xiang et al. (2019), with typical uncertainties of 0.05 dex.

As an important part of SDSS-III/IV, the APOGEE survey (Majewski et al. 2017) has obtained near-infrared (H band; 1.51–1.70 μm) high-resolution ($R\sim22500$) spectra for 437,485 unique stars in the latest DR16 (Ahumada et al. 2020). Estimates of $v_{\rm los}$, the stellar atmospheric parameters, and 20 different elemental-abundance ratios are derived from APOGEE spectra by Jönsson et al. (2020). The typical uncertainties are about 0.5 km s^{-1}, 100 K, 0.10 dex, 0.10 dex, and 0.08 dex for $v_{\rm los}$, $T_{\rm eff}$, $\log g$, [Fe/H], and the individual elemental-abundance ratios, respectively.

[9] http://www.lamost.org/dr8/

Table 1
Comparisons of Radial Velocities Between Large-scale Spectroscopic Surveys and Radial Velocity Standard Stars

Surveys	$\Delta v_{\rm los}$(km s^{-1})	s.d. (km s^{-1})	N
GALAH	−0.31	0.52	76
APOGEE	0.28	0.19	18,080
RAVE	0.07	1.37	374
LAMOST	−4.97	3.83	4975

The GALAH survey is a large-scale stellar spectroscopic survey that aims to collect optical (four discrete optical wavelength ranges: 4713–4903 Å, 5648–5873 Å, 6478–6737 Å, and 7585–7887 Å) high-resolution spectra ($R=28{,}000$) for around one million stars, using the HERMES spectrograph mounted on the 3.9 m Anglo-Australian Telescope (AAT) at Siding Spring Observatory (De Silva et al. 2015). In the current work, we adopt information from GALAH DR2 (Buder et al. 2018), which contains estimates of $v_{\rm los}$, stellar atmospheric parameters, and 23 elemental abundances for 342,682 unique stars. The typical internal uncertainties are around 1.1 km s^{-1}, 60 K, 0.17 dex, 0.10 dex, and 0.02–0.10 dex for $v_{\rm los}$, $T_{\rm eff}$, $\log g$, [Fe/H], and different elemental-abundance ratios, respectively, for FGK-type stars with a typical spectral signal-to-noise ratio (S/N) around 40/1 per pixel.

The accuracy, especially the zero-point, of $v_{\rm los}$, is key for selecting HiVel candidates in the current work. We thus cross-match stars observed by the above large-scale surveys (except for SDSS) to the catalog of radial velocity standard stars constructed by Huang et al. (2018). The final adopted values of $v_{\rm los}$ are corrected for the zero-point offsets (listed in Table 1) found using stars in common between those surveys and the catalog of radial velocity standard stars. The targets of the SDSS survey are too faint to match with those of radial velocity standard stars, and therefore we adopt a −7.3 km s^{-1} offset for this correction from Adelman-McCarthy et al. (2008).

2.2. Astrometric Survey

The European Space Agency (ESA) satellite Gaia (Gaia Collaboration et al. 2016) recently released the Early Data Release 3 (EDR3; Gaia Collaboration et al. 2021), which provides astrometric and photometric data for over 1.8 billion sources, with G-band magnitudes ranging from 3 to 21. For parallax measurements, the typical uncertainties are 0.02–0.04 mas, 0.07–0.1 mas, and 0.5–1.4 mas for $G<15$, =17, and ∼20–21, respectively (Gaia Collaboration et al. 2021). For proper-motion measurements, the typical uncertainties are 0.02–0.04 mas yr^{-1}, 0.07–0.1 mas yr^{-1}, and 0.5–1.5 mas yr^{-1} for $G<15$, =17, and ∼20–21, respectively (Gaia Collaboration et al. 2021).

3. Selection of High-velocity Stars

3.1. Coordinate Systems

In this work, we adopt a right-handed Cartesian system, with X toward the direction opposite to the Sun, Y in the direction of Galactic rotation, and Z in the direction of north Galactic pole (NGP); and a Galactocentric cylindrical system, with R the projected Galactocentric distance, increasing radially outwards, ϕ toward the Galactic rotation direction, and Z the same as that

in the Cartesian system. The three velocity components are represented by (U, V, and W) in the Cartesian system and by (V_R, V_ϕ, and V_Z) in the Galactocentric cylindrical system, respectively. We set the local standard of rest ($U_\odot$, $W_\odot$) = (7.01, 4.95)km s^{-1} (Huang et al. 2015), and the $v_{\phi,\odot} = V_\odot + V_c(R_0)$ is set to the value of 252.17 km s^{-1}, yielded by the proper motion of Sgr A* (Reid & Brunthaler 2004) and the adopted value of Galactocentric distance of the Sun $R_0 = 8.34$ kpc from Reid et al. (2014). The Sun is taken to be located above the disk, with $Z_\odot = 25$ pc (Bland-Hawthorn & Gerhard 2016). The main conclusions of this work still hold up if we adopt alternative values of R_0 (e.g., the most recent measurements by GRAVITY Collaboration et al. 2019), $Z_\odot$ (e.g., Siegert 2019), and solar motions (e.g., Schönrich 2012; Eilers et al. 2019; Zhou et al. 2022).

3.2. Distance and Total Velocity

To derive the total velocities for our spectroscopic targets, accurate distances are required. Rather than simply inverting the Gaia EDR3 parallax measurements, we estimate the distance from parallax by a Bayesian approach:

$$P(d|\varpi, \sigma_\varpi) \propto P(\varpi|d, \sigma_\varpi) d^2 P(r), \quad (1)$$

where r is the distance to the GC.

Similar to Bailer-Jones (2015), the likelihood of parallax is given by:

$$P(\varpi|d, \sigma_\varpi) = \frac{1}{\sqrt{2\pi}\sigma_\varpi} \exp \frac{-\left(\varpi - \varpi_{\rm zp} - \frac{1}{d}\right)^2}{2\sigma_\varpi^2}, \quad (2)$$

where ϖ and σ_ϖ are the parallax and its uncertainties from Gaia EDR3, and $\varpi_{\rm zp}$ is the zero-point of the parallax measurement, which is a function of ecliptic latitude, magnitude, and stellar color, and can be easily obtained by the procedure provided by Lindegren et al. (2021).

Similar to McMillan (2018), the density prior $P(r)$ is defined as:

$$P(r) \propto N_1 \exp\left(-\frac{R}{R_1} - \frac{|z|}{z_1}\right) + N_2 \exp\left(-\frac{R}{R_2} - \frac{|z|}{z_2}\right) + N_3 r^{-\alpha}, \quad (3)$$

where R_1/R_2 and z_1/z_2 are the scale length and height of thin/thick disk, respectively. The detailed values of those parameters are taken from McMillan (2018). Here, α represents the power-law index of the inner-halo density profile, and is set to 3.39 (Carollo et al. 2010). N_1, N_2, and N_3 are the normalization factors that are used to ensure the number density ratio of 0.15 (Jurić et al. 2008) between the thick and the thin disk, and of 0.005 (Carollo et al. 2010) between the halo and the thin disk at the solar position.

By using $v_{\rm los}$ from the aforementioned spectroscopic surveys, proper motions from Gaia EDR3, and the distances derived above, one can derive 3D velocities for all of our sample stars. To do so, we cross-match the RAVE DR5, SDSS DR12, LAMOST DR8, APOGEE DR16, and GALAH DR2 targets to Gaia EDR3 using TOPCAT (Taylor 2005) with a matching radius of 3″: 448,459, 712,742, 5,690,576, 428,876, and 339,890 sample stars are found, respectively. The velocities in the Cartesian system (i.e., U, V, and W) and the Galactocentric cylindrical system (i.e., V_R, V_ϕ, and V_Z) are calculated for all sample stars with reliable measurements of $v_{\rm los}$, proper motions, and distances. Uncertainties in these quantities are calculated by propagation of errors. The total velocity $V_{\rm GSR}$ for each star can be easily derived by:

$$V_{\rm GSR} = (V_R^2 + V_\phi^2 + V_z^2)^{\frac{1}{2}}. \quad (4)$$

In total, 84% of the sample stars with reliable distance estimates ($\varpi \geqslant 0.2$ mas and $\sigma_\varpi/\varpi \leqslant 20\%$) have their total velocities derived in the above manner.

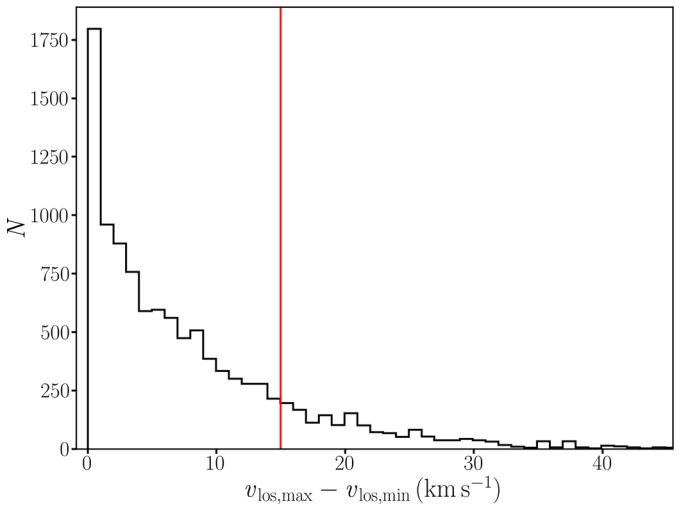

Figure 2. The $v_{\rm los}$ variations (the maximum minus the minimum value) for our 3776 HiVel candidates with multiple observations. For reference, the red-vertical line marks a difference of 15 km s^{-1}.

3.3. HiVel Star Selection

With the total velocity calculated as above, we proceed to construct our HiVel sample. As a first step, we apply the following criteria to the above parent sample to select HiVel candidates with high-quality data:

1. $V_{\rm GSR} \geqslant 300$ km s^{-1};
2. Spectral S/N greater than 10 and uncertainties of $v_{\rm los}$ smaller than 30 km s^{-1};
3. Stellar atmospheric parameters ($T_{\rm eff}$, $\log g$, and [Fe/H]) estimated from spectra;
4. $\varpi \geqslant 0.2$ mas, $\sigma_\varpi/\varpi \leqslant 20\%$ and RUWE < 1.4;
5. Bad spectra are excluded, if found during our visual inspection.

In total, 1406, 3449, 9786, 1264, and 1243 HiVel candidates are found from the RAVE, SDSS DR12, LAMOST, APOGEE, and GALAH surveys, respectively. To exclude multiple entries, the star with the highest spectral S/N is kept if it was observed more than two times within a certain survey, and the entry with the highest spectral resolution (i.e., GALAH, APOGEE, RAVE, SDSS DR12, and finally LAMOST) is kept if the star was observed by two or more spectroscopic surveys. In this way, 14,894 unique stars are obtained. For those 3776 stars with multiple observations, we check their $v_{\rm los}$ variations (the maximum minus the minimum); the result is shown in Figure 2. A total of 837 stars with $v_{\rm los}$ variations larger than 15 km s^{-1} are marked as potential variable/binary stars, and

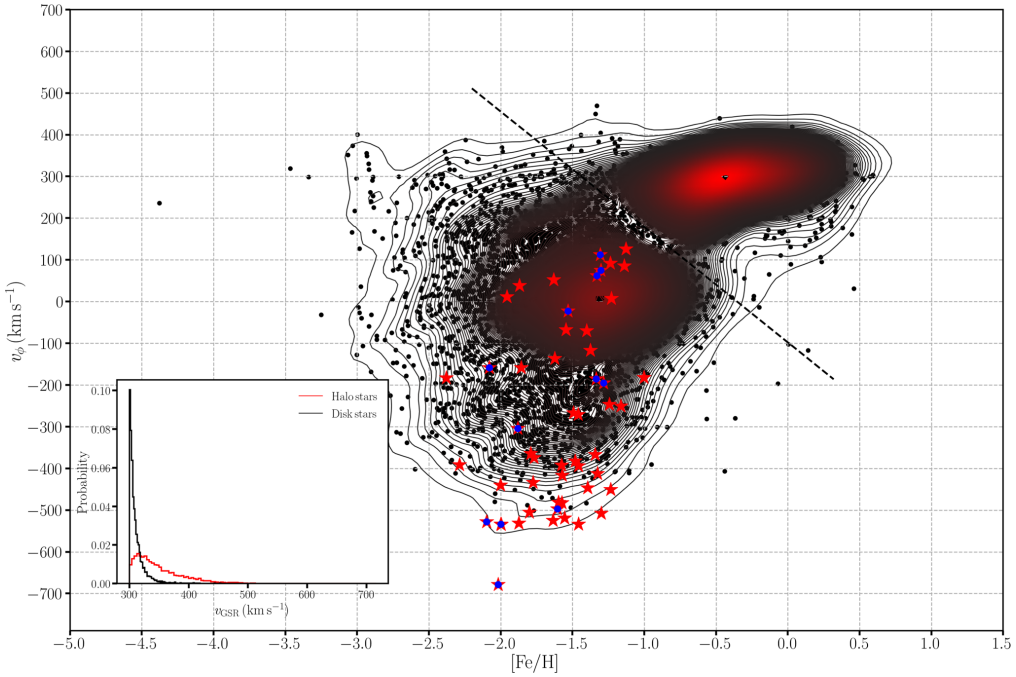

Figure 3. The density distribution of v_ϕ vs. [Fe/H] for our HiVel candidates after the two selection steps. The solid-black lines represent the isodensity contours, and the black-dotted line is the criterion we use to separate the disk population (upper right) and halo population (lower left). The red stars mark the final HVS candidates discovered in this work, some of which (blue-filled circles) were identified by Li et al. (2021). The inset shows the distributions of total velocity, V_{GSR}, for the disk (black) and halo (red) HiVel candidates.

are discarded from our HiVel sample. Most recently, Gaia DR3 has released mean radial velocity measurements for 33 million stars with $G_{RVS} < 14$ mag (Katz et al. 2022). We thus check the radial velocity measurements of our HiVels from ground-based surveys to those from Gaia DR3. In total, 5592 common stars are found. The radial velocities measured from Gaia DR3 are consistent with those measured from the ground-based surveys, with a small offset of only -0.45 km s^{-1} (ground-based minus Gaia) and a tiny scatter of 3.26 km s^{-1}. This check also clearly shows that the previous problems of radial-velocity determinations in Gaia DR2 due to unanticipated alignments between stars, as found by Boubert et al. (2019), have now been largely resolved in Gaia DR3 (Seabroke et al. 2021; Katz et al. 2022).

Second, we search for contamination from (for example) variable stars and white dwarfs with poor v_{los} determinations. We cross-match the HiVel sample to the existing catalogs of variable stars, including the General Catalogue of Variable Stars (Samus' et al. 2017), the Catalina variable catalogs (Drake et al. 2013a, 2013b, 2014, 2017; Torrealba et al. 2015), the ASAS-SN catalogs of variable stars (Shappee et al. 2014; Jayasinghe et al. 2018, 2019a, 2019b), and the Gaia DR2 catalog of variable stars (Gaia Collaboration et al. 2019); 289 potential variable stars are excluded from the HiVel sample. In addition, 208 potential white dwarf candidates (by matching with the white dwarf catalog from Gaia DR2; Gentile Fusillo et al. 2019) in our sample are removed because almost all of them have very poor v_{los} determinations. Two potential M31/M33 member stars are also removed from our HiVel sample.

Following these two steps, over 13,000 HiVel candidates with total velocities $V_{GSR} \geqslant 300$ km s^{-1} remain. We plot them on the V_ϕ–[Fe/H] diagram (Figure 3) to help understand their parent populations. From inspection, there are clearly at least two main clumps: the halo population clustered at low metallicity and $V_\phi \sim 0$ km s^{-1}, and the disk population clustered at high metallicity and $V_\phi = 200$–300 km s^{-1}. We apply an empirical demarcation line, $V_\phi = -276.70 \times$ [Fe/H] -97.78, and classify the candidates into the two populations (disk and halo). With this classification, we then re-calculate the distance estimate for each star by updating the density prior (keep the first two terms for a disk star, and only the last term for a halo star), and then re-estimate the total velocity. We then again apply the HiVel criterion ($V_{GSR} \geqslant 300$ km s^{-1}) to the candidates. By iterating these processes twice, the distance estimate, total velocity calculation, and disk/halo classification converge.

Finally, 12,784 HiVel candidates are selected as our HiVel sample, with 6966 classified as halo stars and 5818 classified as disk stars. As shown in Figure 3, the total velocity distributions of halo and disk HiVel stars are quite different. While the number of the disk population drops quickly to nearly zero at $V_{GSR} = 350$ km s^{-1}, the halo population exhibits a long-tailed distribution, extending beyond -500 to -700 km s^{-1} in v_ϕ.

To select potential HVS, four models of the Galactic potential, two from Monari et al. (2018) and Deason et al. (2019), and two from the `MilkyWayPotential` and `BovyMWPotential2014` potentials implemented in `Gala` (Price-Whelan et al. 2017), are adopted to estimate the Galactic escape velocities. In addition, one measured escape velocity curve from Williams et al. (2017) is adopted. For each of the HiVels, we perform 2000 Monte Carlo simulations to estimate V_{GSR} by sampling the measurement errors (assuming Gaussian distributions, except for the distance whose distributions directly given by Equation 1). The unbound probability P_{ub} of each star is then calculated by counting the frequency of its V_{GSR} exceeding the Galactic escape velocity curves in the 2000 Monte Carlo simulations. In this way, five groups of P_{ub} can be obtained for each star using the five Galactic escape velocity curves mentioned above. As shown in Figure 4 and Table 2, a total of 52 HVS candidates with at least

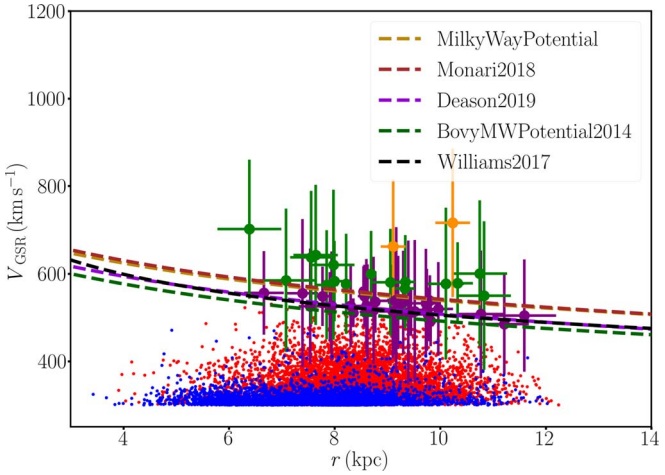

Figure 4. Distribution of the sources of our final HiVel sample in the plane of V_{GSR} and Galactocentric distance r. Red dots denote the halo population and blue dots denote the disk population. The dashed line is the Galactic escape velocity curve. The large dots with $\pm1\sigma$ error bars represent the 52 HVS candidates with at least one group of $P_{ub} \geqslant 50\%$, calculated from Monte Carlo simulations assuming the model Galactic escape velocity curves (dashed lines) derived from different Milky Way's potentials or the measured one (black-dashed line), as indicated in the top right-hand corner. The green and yellow large dots mark those candidates with all five groups of P_{ub} greater than 50 and 80%, respectively.

one group of $P_{ub} \geqslant 50\%$ were found (40 for the first time, and 12 reported by Bromley et al. 2018; Li et al. 2021). We note that these 52 stars are only marginally unbound to the Milky Way's potential. Most of them have unbound probabilities that are smaller than 1σ and only six stars show $P_{ub} > 68\%$ if adopting the Milky Way potential with the largest escape velocities, i.e., `MilkyWayPotential`. Among these, 19 candidates have all five groups of $P_{ub} \geqslant 50\%$ (5 reported by Li et al. 2021). More interestingly, all of these candidates are metal-poor α-enhanced halo stars (see the insets of Figures 1 and 3). Both the $\log g$–T_{eff} diagram and the diagram of absolute magnitude (M_G) versus color ($G_{BP} - G_{RP}$) further indicate that most of those HVS candidates are old turn-off stars with ages roughly between 9–14 Gyr (see Figure 5). Moreover, Figure 6 shows that all the HVS candidates are distributed in the high-Galactic latitude regions.

Detailed information for our newly discovered HVS candidates, as well as those collected from the literature (numbering 88 in total), is listed in Table A1.

4. Comparisons with Other Work

Du et al. (2018) presented a sample of 24 HiVel candidates with $V_{GSR} \geqslant 0.85 V_{esc}$ from LAMOST DR5 and Gaia DR2. From cross-matching our HiVel sample with theirs, nine stars are found in common. The other 15 stars are not in our sample because they are excluded by our cuts: one star with relative parallax uncertainty larger than 20%, nine stars with parallax smaller than 0.2 mas, one star with v_{los} variation larger than 15 km s^{-1}, three stars with RUWE $\geqslant 1.4$, and one star with $V_{GSR} < 300$ km s^{-1}.

For stars in common, the distances adopted by Du et al. (2018) are systematically larger, by over 20%, than those used in the current work. The main reason for this is that in Du et al. (2018) the distances were determined from Gaia DR2 parallaxes with the official zero-point corrections. As shown by Schönrich et al. (2019) and Zinn et al. (2019), the official Gaia DR2 parallax zero-point of 0.029 mas, found by quasars (Lindegren et al. 2018), is smaller than the value of about 0.05 mas found for bright stars. Given the bright nature of the LAMOST targets, the zero-point offset adopted by Du et al. (2018) is not sufficient, and thus the derived distances and velocities are overestimated. We also note that all nine of the stars in common are not HVS candidates.

Most recently, Li et al. (2021, hereafter Li21) presented 591 HiVel candidates with total velocity (V_{GSR}) greater than 445 km s^{-1}, selected from LAMOST DR7 and Gaia DR2. Among those 591 HiVel candidates, 249 stars are found in our sample (including 12 classified as HVS candidates[10]; see the blue-filled circles in Figure 3). The remaining 342 stars are excluded by our various cuts (i.e., 125 stars either not included in LAMOST DR8 or without stellar parameters determined, six stars with spectral S/N smaller than 10, five stars with bad spectra excluded by visual checks, 159 stars with parallax smaller than 0.2 mas, one star with relative parallax uncertainty larger than 20%, one star with radial velocity uncertainty larger than 30 km s^{-1}, nine stars with v_{los} variation larger than 15 km s^{-1}, five stars classified as variable stars, 14 stars with RUWE $\geqslant 1.4$, and 17 stars with total velocity $V_{GSR} < 300$ km s^{-1}). For the stars in common, the total velocities yielded by Li21 are systematically larger than those derived in the current work, mainly due to their distances estimated directly by inverting Gaia DR2 parallax (without zero-point corrections).

In addition to the above searches, several other systematical searches purely based on Gaia DR2 have also reported hundreds of HiVel/HVS candidates (Bromley et al. 2018; Hattori et al. 2018; Du et al. 2019; Marchetti et al. 2019; Li et al. 2020; Marchetti 2021; Reggiani et al. 2022; Quispe-Huaynasi et al. 2022; Liao et al. 2023). Comparing our sample with those candidates, we find three (including one star, LG-HVS35, which is also included in Li21; see above), three, one, and five candidates in common with Bromley et al. (2018), Hattori et al. (2018), Du et al. (2019) and Li et al. (2020), respectively. It is interesting to note that two of our Hivel stars with V_{GSR} no more than 380 km s^{-1} were recently observed by high-resolution spectroscopy by Reggiani et al. (2022). The metallicity and [α/Fe] used in this work are consistent with those measured from high-resolution spectroscopy of Reggiani et al. (2022).

5. Probable Origins of Extreme Velocity Stars

As shown in Figures 1 and 3, all of the HVS candidates discovered in the present work are old, metal-poor, [α/Fe]-enhanced, late-type halo stars. In contrast, the known HVSs in the literature are mostly early-type, massive young stars, largely found from extreme radial velocity only. Moreover, Figure 1 clearly shows that the ejection ratios of these late-type HVS candidates are systematically lower than those of the early-type stars. These properties suggest that the previously known HVSs (early-type) and our new HVS candidates (late-type) may have different ejection mechanisms. One of the explanations of this is that these HVS candidates are actually extreme bound halo stars, as proposed by Hattori et al. (2018). Therefore, these stars can be used to constrain the Galactic potential. To constrain other possible origins of the late-type HVS candidates, we perform backward orbital integration in a model Galactic potential with the

[10] One (LG-HVS35) of the 12 HVS candidates was actually first discovered by Bromley et al. (2018).

Table 2
The 52 HVS Candidates Assuming Different Escape Velocity Curves

Notation Gaia ID	R.A. Decl. (deg)	$\mu_{\alpha}\cos\delta$ $\sigma_{\mu_{\alpha}\cos\delta}$ (mas yr^{-1})	μ_{δ} $\sigma_{\mu_{\delta}}$ (mas yr^{-1})	$v_{\rm los}$ $\sigma_{v_{\rm los}}$ (km s^{-1})	d σ_{d} (kpc)	$V_{\rm GSR}$ $\sigma_{V_{\rm GSR}}$ (km s^{-1})	$P_{\rm ub}$ (MW)[a]	$P_{\rm ub}$ (M18)[b]	$P_{\rm ub}$ (D19)[c]	$P_{\rm ub}$ (BMW)[d]	$P_{\rm ub}$ (W17)[e]
LG-HVS1	12.362361	11.129	−59.488	−345.370	2.328	535.012	0.46	0.45	0.58	0.65	0.59
2556679991337823488	7.128955	0.087	0.078	9.480	0.467	117.951					
LG-HVS2	12.509631	48.314	1.221	−32.940	2.711	517.589	0.40	0.39	0.54	0.61	0.55
2801887851883799936	21.420701	0.065	0.039	14.380	0.438	93.602					
SG-HVS3	29.303224	−15.182	−38.759	217.004	2.458	507.086	0.30	0.29	0.49	0.59	0.50
2510946771548268160	1.193651	0.071	0.056	2.256	0.426	61.543					
LG-HVS4	35.653263	75.919	10.855	151.050	1.515	511.539	0.27	0.26	0.48	0.61	0.49
87667257538859264	21.079511	0.089	0.067	9.470	0.183	53.377					
LG-HVS5	37.488910	57.169	−40.756	−263.450	2.764	716.088	0.92	0.91	0.96	0.97	0.96
2503400067332349440	3.130835	0.065	0.055	18.680	0.539	169.393					
LG-HVS6	54.010210	32.181	−26.060	67.550	3.576	504.377	0.45	0.44	0.55	0.60	0.55
237369721329578112	41.872442	0.053	0.039	13.920	0.697	128.468					
SG-HVS7	62.335793	−21.928	−86.078	16.314	1.519	532.706	0.48	0.47	0.58	0.64	0.59
45249542048091392	15.531954	0.182	0.125	3.303	0.320	124.369					
LG-HVS8	84.087702	75.773	−54.534	−118.040	1.596	492.411	0.22	0.21	0.41	0.51	0.42
263868123355334784	53.192993	0.049	0.040	14.120	0.133	57.819					
SG-HVS9	107.714100	−39.266	−70.707	−43.470	1.711	519.621	0.43	0.42	0.54	0.59	0.54
946735552249457152	39.286968	0.091	0.080	1.811	0.300	107.155					
SG-HVS10	111.533120	46.016	−46.600	−118.499	2.556	600.593	0.68	0.67	0.77	0.81	0.77
897267428899789440	36.689452	0.080	0.064	1.912	0.563	166.708					
SG-HVS11	122.591610	−0.332	−59.917	−33.970	2.804	549.726	0.54	0.54	0.63	0.67	0.64
921561993012731648	40.652329	0.065	0.043	3.204	0.599	169.475					
SG-HVS12	141.546960	−17.158	−33.579	223.547	3.767	484.930	0.37	0.36	0.47	0.52	0.47
694458695225567872	27.340210	0.051	0.037	2.035	0.699	115.507					
SG-HVS13	147.216280	11.123	−128.292	75.051	1.177	514.638	0.22	0.20	0.47	0.63	0.50
1050729011271507328	60.705308	0.039	0.051	2.637	0.069	39.607					
SG-HVS14	149.660010	39.411	−23.042	38.188	2.849	578.540	0.69	0.67	0.83	0.88	0.84
803054228887217024	38.134845	0.050	0.045	3.035	0.469	92.671					
LG-HVS15	154.757012	−17.830	−40.305	−134.730	3.542	507.821	0.43	0.42	0.53	0.57	0.53
809462835487742080	45.733809	0.044	0.055	19.400	0.715	145.156					
SG-HVS16	166.340900	43.549	−18.727	313.306	2.397	599.505	0.71	0.69	0.84	0.90	0.85
3559325645434651648	−17.070308	0.088	0.064	2.566	0.461	97.656					
SG-HVS17	167.381140	−24.318	−36.315	439.254	3.754	662.136	0.82	0.81	0.90	0.93	0.91
3559089525313289344	−17.284739	0.055	0.045	3.208	0.795	152.825					
LG-HVS18	169.502405	−36.101	4.092	157.240	3.097	537.966	0.50	0.48	0.71	0.81	0.73
3998883554967849216	28.818153	0.050	0.081	16.140	0.392	58.385					
LG-HVS19	170.792361	−35.643	−35.437	34.180	3.359	577.195	0.59	0.59	0.68	0.72	0.69
770479307125812864	40.248147	0.055	0.058	15.530	0.741	173.473					
LG-HVS20	180.581777	−36.995	−32.226	26.330	3.191	513.930	0.41	0.40	0.50	0.54	0.50
4026489543162246912	31.837635	0.074	0.055	19.690	0.711	162.690					
SG-HVS21	189.653260	−43.531	−7.011	−66.739	3.196	534.394	0.45	0.43	0.56	0.63	0.57
1514459756956334720	32.344768	0.057	0.056	3.493	0.547	106.635					
LG-HVS22	191.641073	−23.127	−33.598	−88.910	3.917	510.819	0.42	0.41	0.49	0.53	0.50
1513259266353444992	30.695884	0.049	0.062	11.830	0.860	164.598					
SG-HVS23	191.669490	27.761	−30.708	360.732	1.936	510.891	0.13	0.12	0.34	0.53	0.37
3929069346904353152	13.430034	0.081	0.075	1.581	0.264	32.834					

Table 2
(Continued)

Notation Gaia ID	R.A. Decl. (deg)	$\mu_\alpha \cos\delta$ $\sigma_{\mu_\alpha \cos\delta}$ (mas yr^{-1})	μ_δ σ_{μ_δ} (mas yr^{-1})	$v_{\rm los}$ $\sigma_{v_{\rm los}}$ (km s^{-1})	d σ_d (kpc)	$V_{\rm GSR}$ $\sigma_{V_{\rm GSR}}$ (km s^{-1})	$P_{\rm ub}$ (MW)[a]	$P_{\rm ub}$ (M18)[b]	$P_{\rm ub}$ (D19)[c]	$P_{\rm ub}$ (BMW)[d]	$P_{\rm ub}$ (W17)[e]
SG-HVS24	191.991830	−41.337	−51.052	81.992	2.421	540.108	0.49	0.48	0.56	0.60	0.57
1567338780126678400	48.967882	0.062	0.080	1.482	0.558	165.635					
SG-HVS25	192.498020	−52.733	−67.243	−168.672	1.900	536.101	0.41	0.39	0.60	0.69	0.62
1520968079814522496	38.947287	0.030	0.032	2.317	0.176	69.351					
LG-HVS26	194.347116	−7.334	−51.745	175.760	2.876	526.631	0.39	0.38	0.50	0.57	0.51
3942455900972145152	20.419876	0.069	0.052	12.660	0.466	107.150					
LG-HVS27	194.385615	−16.537	−43.399	−221.790	3.587	581.297	0.64	0.62	0.77	0.82	0.78
1517369756214955008	37.110194	0.023	0.026	15.930	0.510	106.325					
LG-HVS28	196.007951	−5.770	−38.240	−154.570	3.847	514.009	0.37	0.36	0.49	0.56	0.50
1461216666591966336	28.552378	0.037	0.051	11.840	0.620	106.636					
LG-HVS29	200.292967	−74.467	−56.547	−58.030	1.833	576.624	0.56	0.54	0.68	0.75	0.69
3938867537399911680	18.835966	0.088	0.051	10.990	0.261	114.295					
LG-HVS30	201.229653	−31.015	−40.112	380.200	2.554	526.695	0.38	0.37	0.50	0.57	0.51
1442286920356579712	20.939786	0.085	0.057	7.650	0.572	94.598					
LG-HVS31	203.794513	−43.676	−9.073	238.430	3.071	524.692	0.32	0.31	0.46	0.55	0.48
3725682648069934336	8.899663	0.049	0.028	14.730	0.430	79.089					
SG-HVS32	204.084080	−45.700	−6.408	33.257	3.563	620.146	0.65	0.64	0.73	0.77	0.73
3726042154012422656	10.005512	0.068	0.048	2.925	0.815	171.275					
LG-HVS33	206.252711	15.691	−29.640	−104.200	3.748	566.398	0.61	0.60	0.78	0.86	0.79
1503968702337282048	46.596244	0.030	0.038	16.340	0.539	78.929					
SG-HVS34	207.085230	16.371	−54.602	216.560	2.027	559.244	0.52	0.50	0.75	0.86	0.78
1500305198313028224	40.949577	0.048	0.060	1.558	0.283	58.227					
LG-HVS35	214.976283	−42.857	−17.186	−245.320	3.358	549.047	0.47	0.45	0.64	0.74	0.66
1484524973071001984	37.669366	0.023	0.029	14.680	0.345	71.489					
SG-HVS36	216.185130	−27.628	−20.628	−338.217	4.151	506.896	0.26	0.25	0.45	0.57	0.47
1506678826700636544	46.550514	0.020	0.024	1.402	0.395	58.074					
SG-HVS37	217.396790	−3.753	−54.087	−112.495	2.912	582.995	0.61	0.59	0.74	0.81	0.75
1280443412952917632	26.915099	0.040	0.039	2.455	0.371	91.517					
SG-HVS38	218.817840	−47.200	−36.613	−237.299	2.679	548.674	0.41	0.39	0.61	0.71	0.62
1242022529603565440	21.728278	0.026	0.031	1.963	0.256	67.944					
LG-HVS39	224.735948	7.222	−29.369	−186.540	4.389	580.327	0.60	0.59	0.71	0.78	0.72
1587301410160177920	46.728570	0.046	0.054	13.830	0.905	121.657					
LG-HVS40	224.807592	−16.170	−65.173	−66.600	2.279	525.834	0.39	0.38	0.48	0.54	0.49
1188512524199896064	17.866868	0.063	0.087	15.610	0.426	131.915					
LG-HVS41	226.584048	−2.004	−43.521	−131.440	3.855	642.758	0.72	0.72	0.80	0.84	0.81
1264622956753148416	24.765407	0.036	0.050	16.960	0.803	160.073					
SG-HVS42	227.154450	3.842	−30.310	−211.830	4.091	538.205	0.46	0.45	0.57	0.63	0.58
1592830751057210496	51.533092	0.051	0.058	2.178	0.906	122.536					
SG-HVS43	227.350790	−42.685	11.386	38.323	3.395	637.638	0.71	0.70	0.80	0.84	0.80
1263758598878844288	23.835252	0.059	0.072	2.909	0.780	151.478					
SG-HVS44	229.492430	−38.172	−15.989	−269.744	3.887	584.788	0.53	0.53	0.61	0.67	0.62
1208146095315810944	16.324317	0.069	0.056	4.129	0.905	163.723					
SG-HVS45	232.301250	−5.243	−42.533	−189.458	3.008	513.102	0.36	0.36	0.47	0.54	0.49
1594746199095755520	50.496393	0.063	0.075	3.028	0.560	108.323					
LG-HVS46	234.156763	5.004	−38.522	16.630	4.504	701.442	0.80	0.79	0.88	0.91	0.89
1164837294370596992	9.002340	0.043	0.044	8.130	0.900	158.662					

Table 2
(Continued)

Notation Gaia ID	R.A. Decl. (deg)	$\mu_{\alpha}\cos\delta$ $\sigma_{\mu_{\alpha}\cos\delta}$ (mas yr^{-1})	μ_{δ} $\sigma_{\mu_{\delta}}$ (mas yr^{-1})	$v_{\rm los}$ $\sigma_{v_{\rm los}}$ (km s^{-1})	d σ_{d} (kpc)	$V_{\rm GSR}$ $\sigma_{V_{\rm GSR}}$ (km s^{-1})	$P_{\rm ub}$ (MW)[a]	$P_{\rm ub}$ (M18)[b]	$P_{\rm ub}$ (D19)[c]	$P_{\rm ub}$ (BMW)[d]	$P_{\rm ub}$ (W17)[e]
SG-HVS47	236.220050	−39.882	13.278	87.606	2.953	556.258	0.42	0.40	0.54	0.61	0.55
4429852530637477760	7.130787	0.064	0.051	4.646	0.545	95.418					
SG-HVS48	241.981170	−14.429	−32.566	−282.395	3.724	516.436	0.39	0.38	0.49	0.54	0.49
1403645069530607616	51.582219	0.063	0.082	3.099	0.760	122.287					
SG-HVS49	252.688090	−6.120	−38.142	−126.759	3.373	526.380	0.40	0.39	0.49	0.56	0.50
1356298174692911104	41.324670	0.056	0.066	2.774	0.707	124.488					
SG-HVS50	319.051060	2.739	−66.662	−303.651	2.293	555.367	0.47	0.46	0.54	0.57	0.55
2689713751472944384	0.499367	0.104	0.086	4.087	0.551	169.175					
SG-HVS51	338.674800	−17.371	−48.307	−167.527	3.001	574.382	0.55	0.53	0.64	0.71	0.66
2609260664602088704	−8.696933	0.056	0.058	2.838	0.528	124.625					
SG-HVS52	341.939260	36.388	−5.165	−91.327	3.357	520.554	0.29	0.28	0.52	0.66	0.55
1888115422016149248	31.152207	0.020	0.025	2.790	0.292	48.674					

Notes.
[a] Unbound probability calculated from the Galactic escape velocity curve under the Milky Way's potential `MilkyWayPotential` implemented in `Gala`;
[b] Unbound probability calculated from the Galactic escape velocity curve under the Milky Way's potential adopted from Monari et al. (2018);
[c] Unbound probability calculated from the Galactic escape velocity curve under the Milky Way's potential adopted from Deason et al. (2019);
[d] Unbound probability calculated from the Galactic escape velocity curve under the Milky Way's potential `BovyMWPotential2014` implemented in `Gala`;
[e] Unbound probability calculated from the Galactic escape velocity curve derived by Williams et al. (2017).

(This table is available in machine-readable form.)

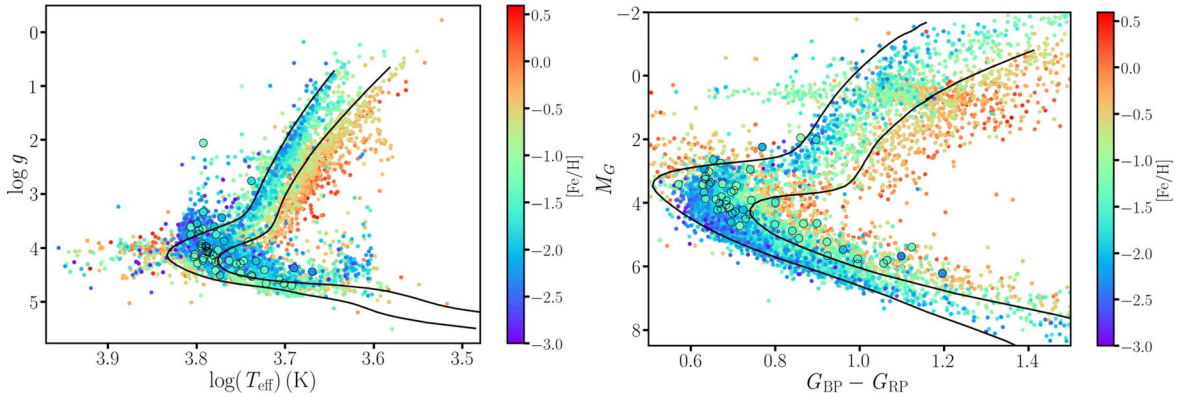

Figure 5. The final HiVel sample shown in the log g–$T_{\rm eff}$ diagram (left-hand panel) and the diagram of M_{G_0} vs. color $(G_{\rm BP}-G_{\rm RP})_0$ (right-hand panel). The color is coded by metallicity, as labeled in the respective right sides. The larger dots are HVS candidates. The two solid lines in the panels represent stellar isochrones from PARSEC (Bressan et al. 2012; Marigo et al. 2017), with [M/H] = −1.85 and age = 9 Gyr for the left-hand line in each panel, and [M/H] = −0.60 and age = 14 Gyr for the right-hand line in each panel.

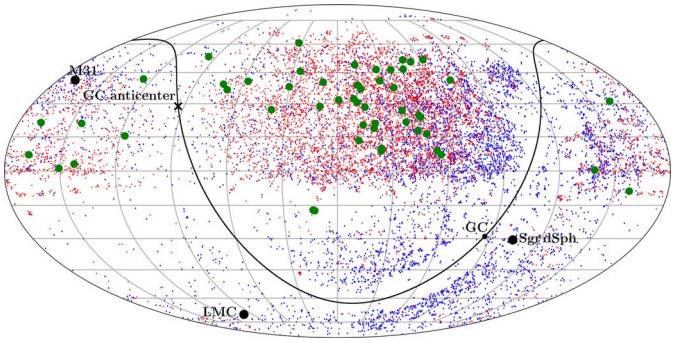

Figure 6. Hammer projection in R.A. and decl. of the final HiVel stars. Blue dots denote the disk population, red dots the halo population, and green-solid circles indicate our HVS candidates. The thick black line indicates the disk plane of the MW, with the large black dot and X-symbol marking the locations of the Galactic center and anticenter, respectively. The locations of M31, the LMC, and the Sgr dSph are also marked with their respective annotations.

package `Gala` for the 547 extreme velocity stars with $V_{\rm GSR} \geqslant 0.8V_{\rm esc}$ ($V_{\rm esc}$ is taken from Williams et al. 2017) in our sample (with only 15 of them classified as disk stars). In Section 5.3, we will also explore the low-velocity portion of our HiVel sample (namely, $300\,{\rm km\,s^{-1}} \leqslant V_{\rm GSR} < 0.8V_{\rm esc}$). The Galactic potential of the MW adopted here is `MilkyWayPotential` in `Gala`, consisting of four components, a nucleus, a bulge, a disk, and a dark matter halo. The details of the four components are described in Bovy (2015). In the orbit integration, a time step of 0.1 Myr is adopted. Our explorations are described in the following three sections.

5.1. Origination from the Galactic Center

We first check whether any of our extreme velocity stars could have been ejected by the Galactic central SMBH via the Hills mechanism. We select those stars whose backward-integrated orbits have their closest distances to the GC smaller than 1 kpc as possible GC-originating candidates. We note that only those candidates during the last pericentric passage through our Galaxy are considered. In total, eight extreme velocity stars are found to have an encounter with the GC within 1 kpc, but none of them are HVS candidates, especially those with highest values of $v_{\rm GSR}$ (i.e., greater than 700 km s^{-1}) that are expected from Hills mechanism (Generozov & Perets 2022). The lack of detections of HVSs with possible GC origins is similar to recent systematic searching efforts with Gaia data (Marchetti et al. 2022). The reason for this is still unclear, but it may due to the small volume covered by Gaia observations due to the requirement of well-measured parallaxes. Table 3 presents the information for those eight stars, including orbital parameters (closest distance and backward time) and their uncertainties yielded from 2000 Monte Carlo trajectory calculations based on observational errors. The backward-integrated orbits are shown in the left-hand panel of Figure 7. By considering the observational uncertainties, we perform Monte Carlo simulations to infer the distribution in the X-Y plane of each star during its intersection of the Galactic plane ($Z = 0$), under the assumption of GC origin. The resulted contours of those candidates, corresponding to the 90% confidence level, are shown in the right-hand panel of Figure 7. We note that the contour of one extreme velocity star, LG-HiVel 11799, is very close to the GC.

Here, only eight extreme velocity stars with $V_{\rm GSR}$ no more than 500 km s^{-1} are found to have had an encounter to the GC within 1 kpc. However, normal halo stars can naturally pass through the GC according to their velocity dispersion. We thus perform a Monte Carlo simulation to evaluate the possibility of normal passages through the GC for halo stars with high velocity. Doing so, one million halo stars are assumed uniformly distributed in a (5 kpc)^3 cubic space of X, Y, and Z, with 3D velocities following the distributions of local halo stars constructed by Anguiano et al. (2020). Similar to the above analysis, we perform backward orbital calculations for 16,041 extremely high-velocity simulated stars with $V_{\rm GSR} \geqslant 0.8V_{\rm esc}$. In total, 1342 of them are found to have a close encounter to the GC within 1 kpc. The derived fraction of 8.37% (1342/16041) is even higher than the observed fraction of 1.46% (8/547), indicating that the eight extreme velocity stars with close encounters to the GC are probably normal halo stars passing through the GC by chance rather than having been ejected by interaction with the SMBH in the GC.

5.2. Origination from the Sgr dSph

To further explore other origins of these extreme velocity stars, we integrate the backward trajectories for the following star clusters and dwarf galaxies: 1743 open clusters with full 6D information and [Fe/H] from Dias et al. (2021); 147 Globular clusters with [Fe/H] from Harris (2010), radial velocities from Vasiliev (2019), proper motions from Vasiliev & Baumgardt (2021), and distances from Baumgardt & Vasiliev (2021);

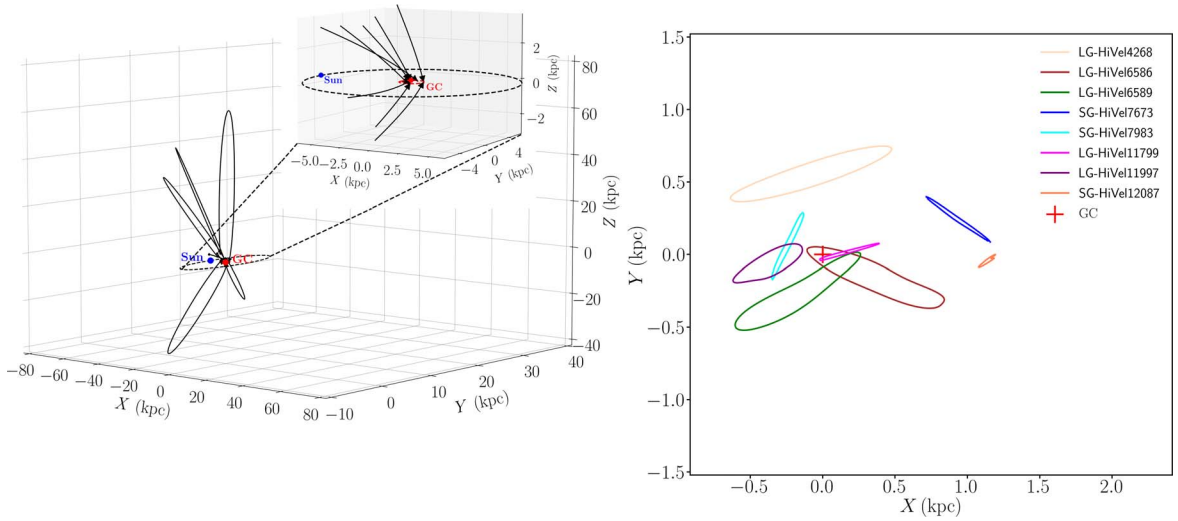

Figure 7. Left-hand panel: A 3D representation of the backward-integrated orbits of eight HiVel stars passing within 1 kpc near the GC. The positions of the Sun and the GC are represented by the blue and red dots, respectively. The Solar circle ($R = 8.34$ kpc) is represented by the dashed circle. Right-hand panel: 90% confidence region of eight HiVel stars in the Galactic plane (X–Y).

Table 3
Eight HiVel Pass Through the Galactic Plane Within 1 kpc of the GC

Notation Gaia ID	R.A. Decl. (deg)	$\mu_\alpha \cos\delta$ $\sigma_{\mu_\alpha \cos\delta}$ (mas yr^{-1})	μ_δ σ_{μ_δ} (mas yr^{-1})	$v_{\rm los}$ $\sigma_{v_{\rm los}}$ (km s^{-1})	d σ_d (kpc)	$V_{\rm GSR}$ $\sigma_{V_{\rm GSR}}$ (km s^{-1})	Closest Distance $\sigma_{\rm Closest\ Distance}$ (kpc)	Backward Time $\sigma_{\rm Backward\ Time}$ (Myr)
LG-HiVel4268	193.531234	−40.214	−0.964	107.820	2.804	441.795	0.64	16.3
3934608033650104320	16.571303	0.049	0.050	14.730	0.344	57.339	0.42	1.2
LG-HiVel6586	224.735724	5.904	−25.086	−196.640	3.998	431.806	0.04	878.2
1268258491950103936	26.419553	0.043	0.046	16.890	0.777	80.058	3.80	390.0
LG-HiVel6589	224.766129	−27.429	11.510	−94.390	3.226	430.846	0.37	14.7
1262339339821422464	22.203286	0.049	0.048	16.310	0.504	60.393	0.38	1.5
SG-HiVel7673	237.236130	5.080	−32.384	−142.706	3.573	460.369	0.83	1114.2
1203663558210616448	18.710947	0.040	0.040	2.746	0.679	95.586	3.03	484.0
SG-HiVel7983	241.245110	6.620	−49.239	3.726	2.270	444.759	0.16	858.8
1199253206614529280	16.786948	0.054	0.061	1.629	0.391	81.117	3.43	412.0
LG-HiVel11799	324.655200	−19.278	−18.812	−291.440	3.851	436.822	0.06	905.0
1767040049125735168	12.585961	0.039	0.036	9.570	0.582	69.724	3.96	404.0
LG-HiVel11997	330.291232	21.953	9.201	−129.920	3.420	418.858	0.11	16.5
1782324257184332032	21.134740	0.049	0.039	14.720	0.509	53.527	0.37	1.3
SG-HiVel12087	333.417060	−37.310	−29.114	−346.033	2.162	490.319	0.70	2853.4
1782213107726332288	22.600503	0.052	0.049	2.919	0.269	56.338	3.91	1400.0

(This table is available in machine-readable form.)

39 dwarf galaxies with full 6D information from Fritz et al. (2018); and for the LMC and SMC (Patel et al. 2020).

Possible links in the trajectories between the extreme velocity stars and the above Galactic subsystems are investigated by sorting the ratios of the closest orbital distances to the subsystems radii[11]. For open or globular clusters, a further cut on metallicity difference (between those extreme velocity stars and clusters) smaller than 0.2 dex is applied. As in the above analysis (Section 5.1), we only consider the last encounter between a specific star and a specific subsystem. Interestingly, 15 extreme velocity stars (including two HVS candidates) are found to have close encounters with the Sgr dSph within two times its half-light radius ($r_h = 2.59$ kpc; McConnachie 2012). Similar to previous investigations (Huang et al. 2021; Bhat et al. 2022), the uncertainties of the orbital parameters for each extreme velocity star are derived from the probability distribution functions (PDF) generated by 2000 Monte Carlo trajectory calculations, assuming that the measurement errors of both extreme velocity star and cluster/dwarf galaxy are normally distributed, except for the distance of extreme velocity star (for which the posterior PDF derived in Section 3.2 is used directly). This information, together with their orbital parameters (closest distance and backward time), as well as their uncertainties, of the 15 extreme velocity stars are listed in Table 4.

[11] Here, the radius of a Galactic subsystem that we adopt is as follows: tidal radius for open and globular clusters, normal radius for LMC and SMC, and two times the half-light radius for dwarf galaxies.

Table 4
Extreme Velocity Stars Probably Originating from the Sgr dSph

Notation Gaia ID	R.A. Decl. (deg)	$\mu_\alpha \cos\delta$ $\sigma_{\mu_\alpha \cos\delta}$ (mas yr^{-1})	μ_δ σ_{μ_δ} (mas yr^{-1})	$v_{\rm los}$ $\sigma_{v_{\rm los}}$ (km s^{-1})	d σ_d (kpc)	$V_{\rm GSR}$ $\sigma_{V_{\rm GSR}}$ (km s^{-1})	Closest Distance $\sigma_{\rm Closest\ Distance}$ (kpc)	Backward Time $\sigma_{\rm Backward\ Time}$ (Myr)
LG-HiVel62	2.375881	44.922	45.648	−312.740	1.475	442.620	1.53	43.7
3832060574174132 48	40.684454	0.023	0.021	12.970	0.068	19.154	0.67	2.1
SG-HiVel1348	110.785890	40.379	−31.264	383.674	1.573	421.659	3.80	44.0
8929232928184362 24	32.062197	0.048	0.041	2.568	0.120	12.508	1.04	2.0
SG-HiVel1713	131.827190	40.839	−29.768	457.035	1.411	436.414	3.70	53.4
6101695153644010 24	16.154381	0.051	0.039	2.466	0.104	11.433	1.69	3.3
LG-HiVel2761	162.632256	3.450	−29.152	503.080	1.634	426.484	3.46	56.4
3982465926515084 544	16.764019	0.034	0.026	12.330	0.079	11.959	1.31	3.6
RG-HiVel3317	175.273875	−8.736	0.023	507.865	2.313	416.561	0.76	53.5
3793871060689209 984	−1.545361	0.027	0.016	1.259	0.108	1.140	0.51	2.7
SG-HiVel5496	211.197860	−33.479	−3.457	248.658	3.143	446.331	4.71	40.0
1231404094841937 536	15.718307	0.051	0.037	2.736	0.538	61.237	0.90	3.3
SG-HiVel6195	220.857380	−46.968	−1.443	193.119	2.453	472.287	2.93	40.5
1186023710910901 760	14.893445	0.052	0.041	3.011	0.267	46.884	0.83	2.8
LG-HiVel6293	221.804648	−47.015	−14.298	250.570	2.214	436.291	3.08	50.5
1186213827638356 096	15.009634	0.045	0.044	16.890	0.198	33.787	1.30	3.8
LG-HiVel6479	223.752833	−41.880	−7.281	184.430	2.529	438.804	1.98	45.2
1282270187101294 592	30.321404	0.050	0.056	13.280	0.374	54.743	1.44	3.2
SG-HiVel6578	224.688950	−49.925	−9.999	264.688	2.086	436.114	2.81	51.5
1155161209793409 408	4.451183	0.052	0.052	2.334	0.240	40.068	1.62	4.7
SG-HVS43	227.350790	−42.685	11.386	38.323	3.395	637.638	4.94	29.8
1263758598878844 288	23.835252	0.059	0.072	2.909	0.780	151.478	2.09	3.0
SG-HVS47	236.220050	−39.882	13.278	87.606	2.953	556.258	4.17	36.1
4429852530637477 760	7.130787	0.064	0.051	4.646	0.545	95.418	1.47	4.0
SG-HiVel8799	251.449790	−54.018	2.255	93.628	2.152	491.882	4.74	49.3
4565596694311458 816	21.149876	0.047	0.052	3.257	0.319	67.504	1.03	5.0
SG-HiVel12019	330.868640	4.706	52.478	−317.809	1.722	452.259	2.28	41.9
1962742265496273 920	44.748228	0.084	0.076	2.985	0.271	66.563	1.64	2.8
RG-HiVel12112	334.496042	−19.547	3.082	−491.044	0.618	422.800	2.83	50.0
2626144254057562 112	−5.197000	0.019	0.019	0.917	0.007	0.788	0.39	2.5

(This table is available in machine-readable form.)

As shown in Figures 8 and 9, the backward-integrated orbital analysis suggests that almost all of the 15 extreme velocity stars intersect the trajectory of the Sgr dSph roughly at its latest pericenter (backward time of 39.7 ± 1.9 Myr) orbiting the MW. By assuming their Sgr dSph origin, the stars have ejection velocities ranging from 500 to 900 km s^{-1} when they left the Sgr dSph (see Figure 9). Note that one of the candidates, J1443 + 1453, was already reported by Huang et al. (2021) to be the first HVS candidate originating from the Sgr dSph. With new astrometric measurements from Gaia EDR3, it has a smaller total velocity than that derived from DR2, and thus is no longer a HVS candidate. Remarkably, two new HVS candidates, SG-HVS43 and SG-HVS47, are found to have had close encounters with the Sgr dSph around its pericenter, 29.8 and 36.1 Myr ago, respectively.

Figure 10 shows these 15 extreme velocity stars[12] in the [α/Fe] versus [Fe/H] plane. Half of them exhibit significantly lower [α/Fe] abundance ratios compared to Galactic field stars (Venn et al. 2004), consistent with the distribution of the Sgr stream member stars. There seem to be five other stars (including one HVS candidate) with high [α/Fe] abundances, which is different from that of the Sgr stream member stars. However, we note that their [α/Fe] abundances were measured from low-resolution spectra, either by LAMOST or SEGUE, and thus the typical error to the abundances is 0.10 dex

[12] Note that three of them do not have [α/Fe] measurements.

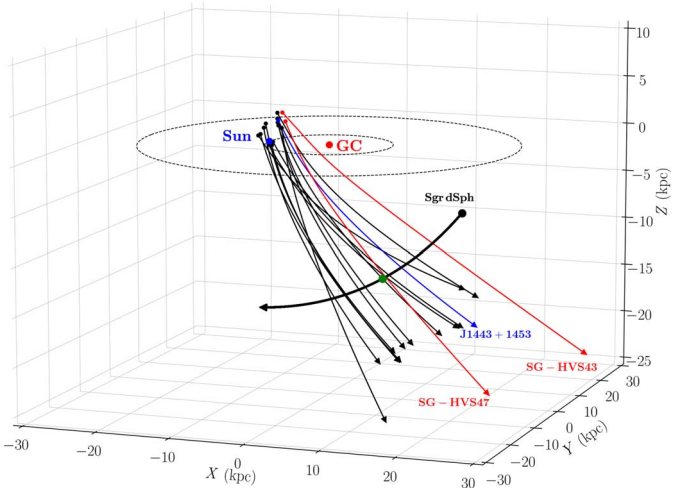

Figure 8. A 3D representation of the backward-integrated orbits for the 15 extreme velocity stars and the Sgr dSph. The present positions of the stars, as well as the Sgr dSph, are marked as black dots. The green dot represents the latest pericenter of the Sgr dSph. The directions of the backward-integrated orbits are denoted by the arrows. The positions of the Sun and the Galactic Center are represented by blue and red dots, respectively. The Solar circle ($R = 8.34$ kpc) and the edge of the MW disk ($R = 25$ kpc) are denoted by the inner and outer dotted lines, respectively. The two red lines denote the backward-integrated orbits of two HVS candidates, SG-HVS43 and SG-HVS47; the blue line indicates the backward-integrated orbit of SG-HiVel6195 (also called J1443+1453), discovered by Huang et al. (2021), which was the first HVS candidate originating from the Sgr dSph.

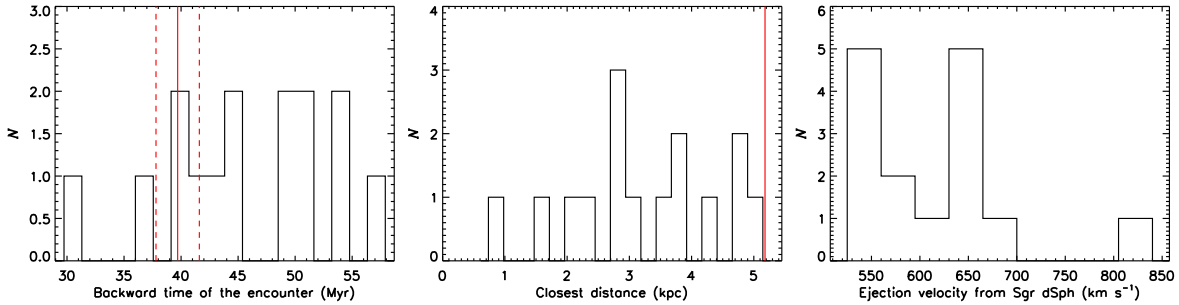

Figure 9. Left-hand panel: The distribution of backward time for the 15 extreme velocity stars that have close encounters with the Sgr dSph within its $2r_h$. The red-solid line indicates the backward time of the Sgr dSph from the present position to its latest pericenter (39.7 Myr), and the red-dashed lines mark its 1σ uncertainty (calculated using the Monte Carlo simulation similar to that described in Section 5.2). Middle panel: The distribution of the closest distances between the 15 stars and the Sgr dSph. The red-solid line denotes two times r_h of the Sgr dSph. Right-hand panel: The distribution of the ejection velocities of the 15 stars, assuming their Sgr dSph origin.

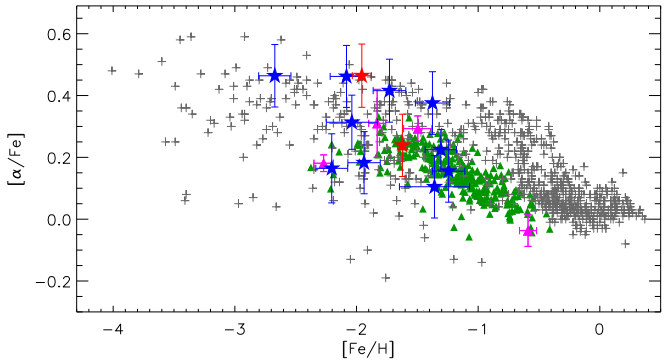

Figure 10. Distributions of the extreme velocity star (blue stars) and HVS candidate (red stars) originating from the Sgr dSph galaxy, Sgr stream member stars (green triangles), Sgr dSph-associated globular clusters (magenta squares), and field stars of the MW (gray-plus symbols) in the [α/Fe]–[Fe/H] plane. The four Sgr dSph-associated globular clusters are M 54, Terzan 7, Terzan 8, and Arp 2, respectively. Their elemental-abundance ratios are measured from high-resolution spectroscopy (Sbordone et al. 2005; Carretta et al. 2010, 2014; Mottini et al. 2008).

(Lee et al. 2011; Xiang et al. 2019). High-resolution follow-up observations are required to clarify the chemical nature of these stars (including the three stars without [α/Fe] measurements), and would be useful to test whether they are ejected from the Sgr dSph or not.

Finally, we note the independent work by Li et al. (2022), following the idea of Huang et al. (2021), who report the discovery of 60 high-velocity star candidates originating in the Sgr dSph, using data from Gaia EDR3 and several massive spectroscopic surveys. The number of high-velocity star candidates in their work is larger than ours, mainly due to our cut on requiring reliable parallax measurements ($\varpi \geqslant$ 0.2 mas). We also note that nine high-velocity RR Lyrae stars were recently identified by Prudil et al. (2022), and two of them are tentatively linked to the Sgr dSph.

In summary, this orbital analysis shows that 15 extreme velocity stars (including 2 HVS candidates) encounter the Sgr dSph within its $2r_h$ radius, when it passes by the latest pericenter of its orbit about the MW. Further analysis in terms of the [α/Fe]–[Fe/H] diagram indicates that at least half of the stars have chemical abundances similar to the Sgr stream member stars and the Sgr dSph-associated globular clusters. As discussed in Huang et al. (2021), such stars are probably stripped from the tidally disrupted Sgr dSph during its latest pericentric passage, which is in agreement with the theoretical predictions by Abadi et al. (2009). Moreover, the properties of this stellar population, together with further numerical simulations, can provide vital constraints on the theory proposed by Abadi et al. (2009). Finally, as mentioned in Huang et al. (2021), a second possibility is that these extreme velocity stars are ejected from the Sgr dSph via the Hills mechanism (Hills 1988), provided that a (central) massive/intermediate-mass black hole resides in the Sgr dSph.

5.3. A General Picture: Tidal Ejection from Galactic Subsystems

The above finding that 15 extreme velocity stars (including two HVS candidates) probably originated from the Sgr dSph has encouraged us to consider a more general picture—tidal ejections of stars from subsystems of our Galaxy can be an important channel to produce extreme velocity stars or even HVSs.

Here, we explore a few more preliminary results for our sample. First, we consider the relatively high-velocity portion of our sample, namely the extreme velocity stars with $V_{\rm GSR} \geqslant 0.8V_{\rm esc}$. As can be seen from inspection of Figure 11, the peak values ($+0.25$ to $+0.30$) of the [α/Fe] distributions of $V_{\rm GSR} \geqslant 0.8V_{\rm esc}$ sources (including HVS candidates) are lower than the value ($+0.40$) found for the Galactic field halo stars. The lower [α/Fe] abundance ratios of those stars are in-line with the chemical-evolution history of dwarf galaxies of the MW (e.g., Tolstoy et al. 2009; Kirby et al. 2011). Certainly, comprehensive numerical simulations (by considering dynamical effects), together with follow-up observations with high-resolution spectroscopy, are required to confirm this general picture and to identify more extreme velocity stars or HVSs (especially the old metal-poor ones) that originated from Galactic subsystems.

We also comment on the sources with relatively lower kinetic energy, i.e., the portion with $300\,{\rm km\,s^{-1}} \leqslant V_{\rm GSR} < 0.8V_{\rm esc}$ in our sample. Their distribution in the [α/Fe]–[Fe/H] diagram is also presented in Figure 11 (see the contours), and is broadly consistent with the extreme velocity star portion. Furthermore, compared with the aforementioned extreme velocity stars, the lower kinetic energy stars have an additional merit that they better reflect the phase-space information of their progenitors. Thus, following the strategy of Helmi et al. (1999), we plot them in the diagram of the total energy ($E_{\rm total}$) versus angular momentum (L_Z), as shown in Figure 12. We have identified the HiVels from our sample that belong to some

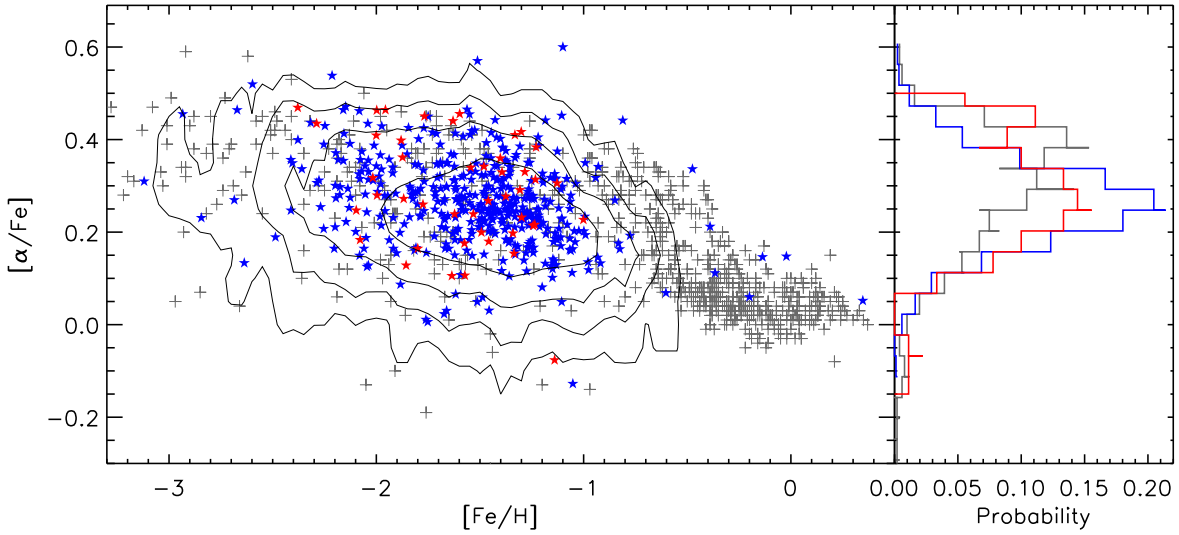

Figure 11. Left-hand panel: Similar to Figure 10, but for all extreme velocity stars (blue stars) with $V_{GSR} \geqslant 0.8V_{esc}$, HVS candidates (red stars), and field stars of the MW (gray pluses). The contours show the number density for the halo HiVels with $V_{GSR} < 0.8V_{esc}$. Right panel: The normalized distributions of [α/Fe] for field halo stars (gray), HVS candidates (red) and extreme velocity stars (blue) with [Fe/H] between −3.3 and −1.0.

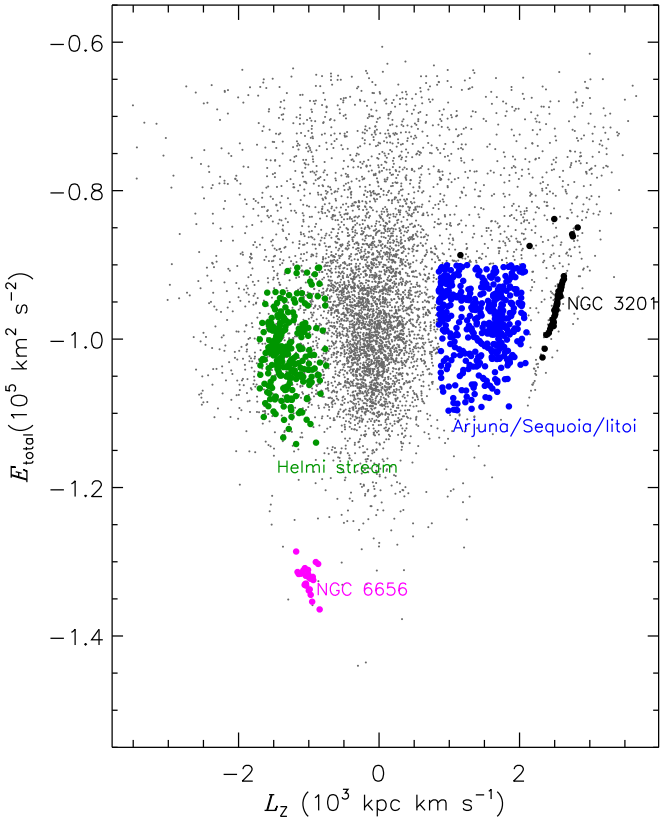

Figure 12. Distribution of the 6434 halo HiVel stars (gray dots) with $V_{GSR} < 0.8V_{esc}$ in the E_{total}–L_Z diagram. We identify and denote some HiVels that belong to certain known Galactic subsystems (see text).

well-known Galactic substructures and star clusters. The member stars of the Helmi stream are identified according to the criteria given by Koppelman et al. (2019), and those of Arjuna/Sequoia/I'itoi are from Naidu et al. (2020).

To identify the members of the globular cluster NGC 3201 and its tidal stream, as well as NGC 6656, we take the following criteria: HiVel stars with line-of-sight velocity and metallicity similar to the given globular cluster, namely $|v_{los} - v_{los}^{cluster}| \leqslant 30$ km s^{-1} and $|[Fe/H] - [Fe/H]^{cluster}| \leqslant 0.3$ dex. The information for the clusters are taken from Harris (2010). These substructures are also shown in Figure 12. We can see that some of our HiVel sources definitely belong to certain known substructures, either simply (once) being the members of globular clusters (e.g., NGC 3201 and NGC 6656), or likely being the accreted debris of certain small systems (e.g., the aforementioned streams). This suggests that we can identify the Galactic-subsystem origins for these lower-velocity HiVel halo stars in the future as larger and more accurate data are acquired.

6. Summary

Based on data from massive large-scale spectroscopic surveys, including the spectra of RAVE DR5, SDSS DR12, LAMOST DR8, APOGEE DR16, and GALAH DR2, and the Gaia EDR3 astrometry, we have assembled a large sample of 12,784 HiVel stars with $V_{GSR} \geqslant 300$ km s^{-1}. Importantly, 52 HVS candidates with total velocity marginally exceeding their local escape velocities are found in this sample, 40 of which are discovered for the first time. More interestingly, all the candidates are late-type metal-poor stars. The properties of these candidates are significantly different from the previous HVSs in the literature, which are generally massive and early-type, and were primarily found by their extreme radial velocities alone.

We perform orbital analyses for 547 extreme velocity stars with $V_{GSR}/V_{esc} \geqslant 0.8$ in our sample to investigate their possible origins. A total of 15 extreme velocity stars (including two HVS candidates) are found to intersect with the orbit of the Sgr dSph within its $2r_h$ around its latest pericentric passage through the MW. Analysis of the [α/Fe]–[Fe/H] diagram indicates that at least half of the 15 stars have chemical abundances similar to the Sgr dSph stars. We have thus sought evidence for the origins of additional HiVels in our sample. After a preliminary analysis, we propose a general picture–star ejection from Galactic subsystems, such as dwarf galaxy and globular clusters, either via tidal stripping or even the Hills mechanism, can be an important channel to produce extreme velocity stars

or even HVSs, particularly the metal-poor late-type population discovered in the present study.

We thank the anonymous referee for their helpful comments. This work is supported by National Natural Science Foundation of China grants 11903027, 11973001, 11833006, 11873083, U1731108, 12090040, 12090044, and National Key R & D Program of China No. 2019YFA0405500. Y.H. is supported by the Yunnan University grant No. C176220100006. T.C.B. acknowledges partial support for this work from grant PHY 14-30152; Physics Frontier Center/JINA Center for the Evolution of the Elements (JINA-CEE), awarded by the US National Science Foundation. H.W.Z. acknowledges the science research grants from the China Manned Space Project with No. CMS-CSST-2021-B03. Z.Y. acknowledges support from the French National Research Agency (ANR) funded project (ANR-18-CE31-0017) and the European Research Council (ERC) under the European Unions Horizon 2020 research and innovation program (grant agreement No. 834148).

The Guoshoujing Telescope (the Large Sky Area Multi-Object Fiber Spectroscopic Telescope, LAMOST) is a National Major Scientific Project built by the Chinese Academy of Sciences. Funding for the project has been provided by the National Development and Reform Commission. LAMOST is operated and managed by the National Astronomical Observatories, Chinese Academy of Sciences. The LAMOST FELLOWSHIP is supported by Special fund for Advanced Users, budgeted and administrated by the Center for Astronomical Mega-Science, Chinese Academy of Sciences (CAMS).

The GALAH survey is based on observations made at the Anglo-Australian Telescope, under programmes A/2013B/13, A/2014A/25, A/2015A/19, A/2017A/18. We acknowledge the traditional owners of the land on which the AAT stands, the Gamilaraay people, and pay our respects to elders past and present.

Funding for the Sloan Digital Sky Survey IV has been provided by the Alfred P. Sloan Foundation, the U.S. Department of Energy Office of Science, and the Participating Institutions. SDSS acknowledges support and resources from the Center for High-Performance Computing at the University of Utah. The SDSS website is www.sdss.org.

Funding for RAVE has been provided by: the Australian Astronomical Observatory; the Leibniz-Institut fuer Astrophysik Potsdam (AIP); the Australian National University; the Australian Research Council; the French National Research Agency; the German Research Foundation (SPP 1177 and SFB 881); the European Research Council (ERC-StG 240271 Galactica); the Istituto Nazionale di Astrofisica at Padova; the Johns Hopkins University; the National Science Foundation of the USA (AST-0908326); the W. M. Keck foundation; the Macquarie University; the Netherlands Research School for Astronomy; the Natural Sciences and Engineering Research Council of Canada; the Slovenian Research Agency; the Swiss National Science Foundation; the Science & Technology Facilities Council of the UK; Opticon; Strasbourg Observatory; and the Universities of Groningen, Heidelberg and Sydney. The RAVE website is at https://www.rave-survey.org.

This work has made use of data from the European Space Agency (ESA) mission Gaia (https://www.cosmos.esa.int/gaia), processed by the Gaia https://www.cosmos.esa.int/web/gaia/dpac/consortium). Funding for the DPAC has been provided by national institutions, in particular the institutions participating in the Gaia Multilateral Agreement.

Appendix
Information of 88 known HVSs or Candidates

In Table A1, we present proper motions, line-of-sight velocities, distances, stellar atmospheric parameters, [α/Fe], radial velocity in the Galactic rest frame $V_{\rm rf}$, and total velocity $V_{\rm GSR}$ for 88 known HVSs or candidates, including the 52 found in this work. For those HVS candidates discovered in this work, the first letter of their names represents the spectroscopic survey used to find this HVS candidates (i.e., L—LAMOST and S—SDSS) and the second letter is always G, indicating the astrometric information from Gaia EDR3. For those HVSs found by Brown et al. (2005, 2006, 2007, 2009, 2012, 2014), the distances and stellar atmospheric parameters are all taken from their final updates (Brown et al. 2014). The distances of the three WD HVSs, found by Shen et al. (2018), are derived by the parallax measurements from Gaia EDR3 by the method mentioned in Section 3.2. For the remaining HVSs or HVS candidates, their information are taken from the references listed in Table A1. The proper motions for all those HVSs or HVS candidates are taken from Gaia EDR3. $V_{\rm rf}$ and $V_{\rm GSR}$ are those calculated by adopting the values of $U_\odot$, $v_{\phi,\odot}$, $W_\odot$ and R_0 described in Section 3.1.

Table A1
Basic Parameters for 88 HVSs or Candidates

ID	Notation Gaia ID	R.A. Decl. (deg)	$\mu_\alpha \cos\delta$ $\sigma_{\mu_\alpha \cos\delta}$ (mas yr^{-1})	μ_δ σ_{μ_δ} (mas yr^{-1})	$v_{\rm los}$ $\sigma_{v_{\rm los}}$ (km s^{-1})	d σ_d (kpc)	$T_{\rm eff}$ $\sigma_{T_{\rm eff}}$ (K)	$\log g$ $\sigma_{\log g}$ (dex)	[Fe/H] $\sigma_{\rm [Fe/H]}$ (dex)	[α/Fe] $\sigma_{\rm [\alpha/Fe]}$ (dex)	$V_{\rm rf}$ $\sigma_{V_{\rm rf}}$ (km s^{-1})	$V_{\rm GSR}$ $\sigma_{V_{\rm GSR}}$ (km s^{-1})	Reference
					HVS Candidates from this Work								
1	LG-HVS1	12.362361	11.129	−59.488	−345.37	2.33	5629	4.29	−1.46	⋯	−231.24	535.01	this work
	2556679991337823488	7.128955	0.087	0.078	9.48	0.47	201	0.32	0.19	⋯	9.48	117.95	
2	LG-HVS2	12.509631	48.314	1.221	−32.94	2.71	6065	4.21	−1.34	+0.15	120.38	517.59	this work[a]
	2801887851883799936	21.420701	0.065	0.039	14.38	0.44	257	0.40	0.24	0.09	14.38	93.60	
3	SG-HVS3	29.303224	−15.182	−38.759	217.00	2.46	5961	4.24	−1.24	+0.22	267.09	507.09	this work
	2510946771548268160	1.193651	0.071	0.056	2.26	0.43	19	0.06	0.03	0.01	2.26	61.54	
4	LG-HVS4	35.653263	75.919	10.855	151.05	1.51	5290	4.41	−1.53	+0.24	244.44	511.54	this work[a]
	87667257538859264	21.079511	0.089	0.067	9.47	0.18	195	0.31	0.18	0.05	9.47	53.38	
5	LG-HVS5	37.488910	57.169	−40.756	−263.45	2.76	5874	3.87	−2.02	+0.32	−230.70	716.09	this work[a]
	2503400067332349440	3.130835	0.065	0.055	18.68	0.54	194	0.32	0.19	0.06	18.68	169.39	
6	LG-HVS6	54.010210	32.181	−26.060	67.55	3.58	5969	4.04	−1.57	+0.18	173.13	504.38	this work
	237369721329578112	41.872442	0.053	0.039	13.92	0.70	55	0.09	0.05	0.04	13.92	128.47	
7	SG-HVS7	62.335793	−21.928	−86.078	16.31	1.52	5463	4.53	−1.38	+0.28	18.31	532.71	this work
	45249542048091392	15.531954	0.182	0.125	3.30	0.32	58	0.11	0.08	0.01	3.30	124.37	
8	LG-HVS8	84.087702	75.773	−54.534	−118.04	1.60	6098	4.08	−1.57	⋯	−31.81	492.41	this work
	263868123355334784	53.192993	0.049	0.040	14.12	0.13	208	0.33	0.19	⋯	14.12	57.82	
9	SG-HVS9	107.714100	−39.266	−70.707	−43.47	1.71	4900	4.37	−2.38	+0.47	−41.10	519.62	this work
	946735552249457152	39.286968	0.091	0.080	1.81	0.30	78	0.10	0.11	0.01	1.81	107.15	
10	SG-HVS10	111.533120	46.016	−46.600	−118.50	2.56	5630	4.46	−1.23	+0.31	−130.90	600.59	this work
	897267428899789440	36.689452	0.080	0.064	1.91	0.56	32	0.05	0.03	0.01	1.91	166.71	
11	SG-HVS11	122.591610	−0.332	−59.917	−33.97	2.80	6223	3.92	−1.87	+0.36	−37.24	549.73	this work
	921561993012731648	40.652329	0.065	0.043	3.20	0.60	35	0.12	0.05	0.01	3.20	169.48	
12	SG-HVS12	141.546960	−17.158	−33.579	223.55	3.77	6201	3.33	−1.77	+0.45	160.23	484.93	this work
	694458695225567872	27.340210	0.051	0.037	2.03	0.70	30	0.04	0.04	0.01	2.03	115.51	
13	SG-HVS13	147.216280	11.123	−128.292	75.05	1.18	4673	4.44	−2.29	+0.43	157.41	514.64	this work
	1050729011271507328	60.705308	0.039	0.051	2.64	0.07	58	0.26	0.10	0.01	2.64	39.61	
14	SG-HVS14	149.660010	39.411	−23.042	38.19	2.85	6163	3.97	−1.23	+0.38	25.01	578.54	this work
	803054228887217024	38.134845	0.050	0.045	3.03	0.47	28	0.13	0.03	0.01	3.03	92.67	
15	LG-HVS15	154.757012	−17.830	−40.305	−134.73	3.54	5998	3.75	−1.60	+0.46	−111.87	507.82	this work
	809462835487742080	45.733809	0.044	0.055	19.40	0.72	354	0.57	0.34	0.14	19.40	145.16	
16	SG-HVS16	166.340900	43.549	−18.727	313.31	2.40	5585	4.24	−1.40	+0.36	120.02	599.51	this work
	3559325645434651648	−17.070308	0.088	0.064	2.57	0.46	44	0.08	0.04	0.02	2.57	97.66	
17	SG-HVS17	167.381140	−24.318	−36.315	439.25	3.75	6304	3.55	−2.00	+0.28	247.00	662.14	this work
	3559089525313289344	−17.284739	0.055	0.045	3.21	0.79	31	0.10	0.05	0.01	3.21	152.83	
18	LG-HVS18	169.502405	−36.101	4.092	157.24	3.10	6296	4.28	−1.13	+0.31	125.14	537.97	this work
	3998883554967849216	28.818153	0.050	0.081	16.14	0.39	174	0.28	0.17	0.05	16.14	58.38	
19	LG-HVS18	170.792361	−35.643	−35.437	34.18	3.36	6044	4.13	−1.57	+0.11	50.23	577.20	this work
	770479307125812864	40.248147	0.055	0.058	15.53	0.74	173	0.28	0.16	0.07	15.53	173.47	
20	LG-HVS20	180.581777	−36.995	−32.226	26.33	3.19	6130	4.07	−1.77	+0.26	24.25	513.93	this work
	4026489543162246912	31.837635	0.074	0.055	19.69	0.71	309	0.48	0.29	0.11	19.69	162.69	
21	SG-HVS21	189.653260	−43.531	−7.011	−66.74	3.20	6209	3.65	−1.28	+0.33	−49.55	534.39	this work[a]
	1514459756956334720	32.344768	0.057	0.056	3.49	0.55	38	0.10	0.02	0.01	3.49	106.64	
22	LG-HVS22	191.641073	−23.127	−33.598	−88.91	3.92	6202	4.20	−1.30	+0.23	−73.63	510.82	this work
	1513259266353444992	30.695884	0.049	0.062	11.83	0.86	58	0.10	0.06	0.04	11.83	164.60	
23	SG-HVS23	191.669490	27.761	−30.708	360.73	1.94	4930	4.70	−1.33	+0.41	313.45	510.89	this work[a]
	3929069346904353152	13.430034	0.081	0.075	1.58	0.26	13	0.09	0.02	0.01	1.58	32.83	
24	SG-HVS24	191.991830	−41.337	−51.052	81.99	2.42	5090	4.59	−1.39	+0.33	162.49	540.11	this work
	1567338780126678400	48.967882	0.062	0.080	1.48	0.56	26	0.04	0.06	0.01	1.48	165.63	
25	SG-HVS25	192.498020	−52.733	−67.243	−168.67	1.90	6129	4.06	−2.00	+0.46	−121.96	536.10	this work[a]
	1520968079814522496	38.947287	0.030	0.032	2.32	0.18	23	0.14	0.04	0.01	2.32	69.35	

Table A1
(Continued)

ID	Notation Gaia ID	R.A. Decl. (deg)	$\mu_\alpha \cos\delta$ $\sigma_{\mu_\alpha \cos\delta}$ (mas yr^{-1})	μ_δ σ_{μ_δ} (mas yr^{-1})	$v_{\rm los}$ $\sigma_{v_{\rm los}}$ (km s^{-1})	d σ_d (kpc)	$T_{\rm eff}$ $\sigma_{T_{\rm eff}}$ (K)	$\log g$ $\sigma_{\log g}$ (dex)	[Fe/H] $\sigma_{\rm [Fe/H]}$ (dex)	[α/Fe] $\sigma_{\rm [\alpha/Fe]}$ (dex)	$V_{\rm rf}$ $\sigma_{V_{\rm rf}}$ (km s^{-1})	$V_{\rm GSR}$ $\sigma_{V_{\rm GSR}}$ (km s^{-1})	Reference
26	LG-HVS26	194.347116	−7.334	−51.745	175.76	2.88	6007	4.42	−1.32	⋯	159.90	526.63	this work
	3942455900972145152	20.419876	0.069	0.052	12.66	0.47	282	0.44	0.26	⋯	12.66	107.15	
27	LG-HVS27	194.385615	−16.537	−43.399	−221.79	3.59	6151	3.97	−2.10	+0.25	−177.83	581.30	this work[a]
	1517369756214955008	37.110194	0.023	0.026	15.93	0.51	38	0.06	0.04	0.05	15.93	106.32	
28	LG-HVS28	196.007951	−5.770	−38.240	−154.57	3.85	6154	4.07	−1.48	+0.34	−137.44	514.01	this work
	1461216666591966336	28.552378	0.037	0.051	11.84	0.62	47	0.08	0.04	0.03	11.84	106.64	
29	LG-HVS29	200.292967	−74.467	−56.547	−58.03	1.83	5475	4.51	−1.55	⋯	−64.88	576.62	this work
	3938867537399911680	18.835966	0.088	0.051	10.99	0.26	251	0.40	0.23	⋯	10.99	114.30	
30	LG-HVS30	201.229653	−31.015	−40.112	380.20	2.55	5269	4.65	−1.34	+0.20	383.05	526.69	this work
	1442286920356579712	20.939786	0.085	0.057	7.65	0.57	284	0.45	0.27	0.09	7.65	94.60	
31	LG-HVS31	203.794513	−43.676	−9.073	238.43	3.07	6341	4.12	−1.16	⋯	206.53	524.69	this work
	3725682648069934336	8.899663	0.049	0.028	14.73	0.43	318	0.49	0.30	⋯	14.73	79.09	
32	SG-HVS32	204.084080	−45.700	−6.408	33.26	3.56	6222	4.00	−1.46	+0.27	5.90	620.15	this work
	3726042154012422656	10.005512	0.068	0.048	2.93	0.81	20	0.08	0.05	0.01	2.93	171.28	
33	LG-HVS33	206.252711	15.691	−29.640	−104.20	3.75	6348	4.16	−1.31	+0.29	−5.82	566.40	this work[a]
	1503968702337282048	46.596244	0.030	0.038	16.34	0.54	156	0.26	0.15	0.07	16.34	78.93	
34	SG-HVS34	207.085230	16.371	−54.602	216.56	2.03	5030	4.66	−1.30	+0.42	299.65	559.24	this work[a]
	1500305198313028224	40.949577	0.048	0.060	1.56	0.28	30	0.09	0.04	0.01	1.56	58.23	
35	LG-HVS35	214.976283	−42.857	−17.186	−245.32	3.36	6238	3.97	−1.60	⋯	−154.56	549.05	this work[b]
	1484524973071001984	37.669366	0.023	0.029	14.68	0.35	214	0.34	0.20	⋯	14.68	71.49	
36	SG-HVS36	216.185130	−27.628	−20.628	−338.22	4.15	5473	2.76	−1.80	+0.16	−220.42	506.90	this work
	1506678826700636544	46.550514	0.020	0.024	1.40	0.39	43	0.87	0.03	0.05	1.40	58.07	
37	SG-HVS37	217.396790	−3.753	−54.087	−112.50	2.91	6408	3.75	−1.88	+0.40	−48.10	582.99	this work[a]
	1280443412952917632	26.915099	0.040	0.039	2.45	0.37	15	0.09	0.03	0.01	2.45	91.52	
38	SG-HVS38	218.817840	−47.200	−36.613	−237.30	2.68	6407	3.61	−1.46	+0.18	−185.33	548.67	this work
	1242022529603565440	21.728278	0.026	0.031	1.96	0.26	37	0.13	0.06	0.01	1.96	67.94	
39	LG-HVS39	224.735948	7.222	−29.369	−186.54	4.39	6004	4.25	−1.14	−0.08	−51.06	580.33	this work
	1587301410160177920	46.728570	0.046	0.054	13.83	0.90	102	0.17	0.10	0.17	13.83	121.66	
40	LG-HVS40	224.807592	−16.170	−65.173	−66.60	2.28	5763	4.03	−1.79	⋯	−10.13	525.83	this work
	1188512524199896064	17.866868	0.063	0.087	15.61	0.43	282	0.44	0.26	⋯	15.61	131.91	
41	LG-HVS41	226.584048	−2.004	−43.521	−131.44	3.85	6114	4.00	−1.49	+0.20	−49.17	642.76	this work
	1264622956753148416	24.765407	0.036	0.050	16.96	0.80	352	0.56	0.33	0.13	16.96	160.07	
42	SG-HVS42	227.154450	3.842	−30.310	−211.83	4.09	5797	4.23	−1.63	+0.44	−61.56	538.21	this work
	1592830751057210496	51.533092	0.051	0.058	2.18	0.91	22	0.07	0.03	0.01	2.18	122.54	
43	SG-HVS43	227.350790	−42.685	11.386	38.32	3.40	6212	4.23	−1.62	+0.24	119.92	637.64	this work
	1263758598878844288	23.835252	0.059	0.072	2.91	0.78	20	0.12	0.04	0.01	2.91	151.48	
44	SG-HVS44	229.492430	−38.172	−15.989	−269.74	3.89	6267	3.66	−1.64	+0.11	−204.84	584.79	this work
	1208146095315810944	16.324317	0.069	0.056	4.13	0.91	46	0.06	0.06	0.01	4.13	163.72	
45	SG-HVS45	232.301250	−5.243	−42.533	−189.46	3.01	5691	4.29	−1.55	+0.34	−31.61	513.10	this work
	1594746199095755520	50.496393	0.063	0.075	3.03	0.56	42	0.03	0.04	0.02	3.03	108.32	
46	LG-HVS46	234.156763	5.004	−38.522	16.63	4.50	5517	3.88	−1.00	+0.23	72.07	701.44	this work
	1164837294370596992	9.002340	0.043	0.044	8.13	0.90	57	0.09	0.05	0.03	8.13	158.66	
47	SG-HVS47	236.220050	−39.882	13.278	87.61	2.95	6030	3.60	−1.96	+0.46	143.06	556.26	this work
	4429852530637477760	7.130787	0.064	0.051	4.65	0.55	42	0.09	0.08	0.02	4.65	95.42	
48	SG-HVS48	241.981170	−14.429	−32.566	−282.39	3.72	6273	3.74	−1.86	+0.13	−105.27	516.44	this work
	1403645069530607616	51.582219	0.063	0.082	3.10	0.76	20	0.14	0.05	0.03	3.10	122.29	
49	SG-HVS49	252.688090	−6.120	−38.142	−126.76	3.37	5938	4.51	−1.87	+0.27	55.59	526.38	this work
	1356298174692911104	41.324670	0.056	0.066	2.77	0.71	14	0.02	0.00	0.01	2.77	124.49	
50	SG-HVS50	319.051060	2.739	−66.662	−303.65	2.29	5407	4.24	−2.00	+0.41	−133.28	555.37	this work
	2689713751472944384	0.499367	0.104	0.086	4.09	0.55	63	0.11	0.05	0.02	4.09	169.17	
51	SG-HVS51	338.674800	−17.371	−48.307	−167.53	3.00	6201	2.06	−1.24	+0.21	−42.54	574.38	this work

Table A1
(Continued)

ID	Notation Gaia ID	R.A. Decl. (deg)	$\mu_\alpha \cos\delta$ $\sigma_{\mu_\alpha \cos\delta}$ (mas yr^{-1})	μ_δ σ_{μ_δ} (mas yr^{-1})	$v_{\rm los}$ $\sigma_{v_{\rm los}}$ (km s^{-1})	d σ_d (kpc)	$T_{\rm eff}$ $\sigma_{T_{\rm eff}}$ (K)	$\log g$ $\sigma_{\log g}$ (dex)	[Fe/H] $\sigma_{\rm [Fe/H]}$ (dex)	[α/Fe] $\sigma_{\rm [\alpha/Fe]}$ (dex)	$V_{\rm rf}$ $\sigma_{V_{\rm rf}}$ (km s^{-1})	$V_{\rm GSR}$ $\sigma_{V_{\rm GSR}}$ (km s^{-1})	Reference
	2609260664602088704	−8.696933	0.056	0.058	2.84	0.53	58	0.69	0.03	0.01	2.84	124.62	
52	SG-HVS52	341.939260	36.388	−5.165	−91.33	3.36	5913	3.44	−2.08	+0.18	134.75	520.55	this work[a]
	1888115422016149248	31.152207	0.020	0.025	2.79	0.29	33	0.07	0.05	0.01	2.79	48.67	
					HVSs or candidates from other literature								
53	J013655.91 + 242546.0	24.232958	−1.820	−6.660	324.00	10.90	9100	3.90	⋯	⋯	456.42	557.94	Tillich et al. (2009)
	291821209329550464	24.429440	0.050	0.041	5.90	2.00	250	0.15	⋯	⋯	5.90	30.35	
54	LAMOST-HVS3	50.321157	1.146	−0.549	361.00	22.32	14000	⋯	⋯	⋯	407.96	428.93	Huang et al. (2017)
	56282900715073664	19.126719	0.082	0.067	12.52	2.50	⋯	⋯	⋯	⋯	12.52	12.23	
55	HVS3(HE 0437-5439)	69.553330	0.853	1.614	723.00	61.00	20354	3.77	⋯	⋯	529.95	747.09	Edelmann et al. (2005)
	4777328613382967040	−54.553300	0.049	0.061	3.00	12.00	360	0.05	⋯	⋯	3.00	69.17	
56	HD 271791	90.616163	−0.413	4.704	441.00	24.00	17810	3.04	⋯	⋯	221.41	569.75	Heber et al. (2008)
	5284151216932205312	−66.791300	0.035	0.042	⋯	2.50	180	0.03	⋯	⋯	⋯	50.48	
57	HVS1	136.937400	−0.604	−0.474	833.00	101.30	11125	3.91	⋯	⋯	673.13	731.61	Brown et al. (2005)
	577294697514301440	2.751950	0.602	0.385	5.50	14.46	463	0.20	⋯	⋯	5.50	109.15	
58	LAMOST-HVS1	138.027170	−3.557	−0.793	620.00	13.40	20700	3.67	−0.13	⋯	483.45	554.21	Zheng et al. (2014)
	590511484409775360	9.272722	0.031	0.027	10.00	2.20	1200	0.19	0.07	⋯	10.00	14.68	
59	HVS4	138.254200	−0.204	−0.601	600.90	63.80	14547	4.15	⋯	⋯	551.94	558.30	Brown et al. (2006)
	6998110791736836928	30.855500	0.263	0.193	6.20	9.99	607	0.21	⋯	⋯	6.20	13.43	
60	HVS5	139.497800	0.001	−0.989	545.50	44.40	12000	3.89	⋯	⋯	653.45	653.87	Brown et al. (2006)
	1069326945513133952	67.377300	0.084	0.105	4.30	5.11	350	0.13	⋯	⋯	4.30	4.48	
61	HVS2(US708)	143.336958	−5.447	1.776	917.00	8.50	47200	5.69	⋯	⋯	927.88	1001.57	Geier et al. (2015)
	815106177700219392	44.284861	0.193	0.164	7.00	1.00	400	0.09	⋯	⋯	7.00	10.10	
62	HVS8	145.558500	−0.877	−0.276	499.30	53.43	11000	3.75	⋯	⋯	407.24	478.67	Brown et al. (2007)
	6335997602588277776	20.056100	0.162	0.144	2.90	9.84	1000	0.25	⋯	⋯	2.90	23.53	
63	HVS9	155.404500	0.265	−0.808	616.80	75.13	11680	3.83	⋯	⋯	455.27	491.18	Brown et al. (2007)
	3830584196322129920	−0.876330	0.427	0.648	5.10	11.76	529	0.21	⋯	⋯	5.10	81.39	
64	HVS21	158.576042	−0.199	−0.652	356.80	108.64	13229	4.16	⋯	⋯	392.90	405.83	Brown et al. (2012)
	834069905715968640	48.192936	0.412	0.650	7.50	21.01	998	0.31	⋯	⋯	7.50	127.82	
65	HVS14	161.007300	−2.166	2.282	537.30	102.19	11030	3.90	⋯	⋯	406.18	1681.51	Brown et al. (2009)
	3859275333773935488	6.194167	1.376	1.684	7.20	16.47	554	0.24	⋯	⋯	7.20	719.69	
66	HVS12	162.540000	0.928	−0.193	552.20	64.54	12098	4.62	⋯	⋯	412.92	565.64	Brown et al. (2009)
	3809777626689513216	3.264080	0.876	0.580	6.60	8.32	632	0.28	⋯	⋯	6.60	175.84	
67	HVS13	163.201300	0.065	−0.203	572.70	104.14	11241	4.04	⋯	⋯	423.34	446.36	Brown et al. (2009)
	3804790100211231104	−0.026090	0.788	0.629	4.50	18.70	739	0.33	⋯	⋯	4.50	177.00	
68	HVS6	166.489400	0.119	0.125	609.40	55.36	12190	4.30	⋯	⋯	498.10	566.23	Brown et al. (2006)
	3867267443277880320	9.577640	0.298	0.231	6.80	7.14	546	0.23	⋯	⋯	6.80	31.84	
69	HVS24	167.901830	0.101	−0.403	496.20	61.80	11103	4.00	⋯	⋯	357.17	383.87	Brown et al. (2014)
	3810351984075984768	0.982333	0.311	0.265	6.80	11.10	806	0.31	⋯	⋯	6.80	33.78	
70	HVS7	173.300500	−0.089	0.020	527.80	52.17	12000	3.80	⋯	⋯	398.54	451.19	Brown et al. (2006)
	3799146650623432704	1.140250	0.183	0.129	2.70	6.49	500	0.10	⋯	⋯	2.70	15.26	
71	HVS15	173.421200	−1.295	−0.483	461.00	61.00	11132	4.05	⋯	⋯	323.82	423.76	Brown et al. (2009)
	3794074603484360704	−1.353940	0.357	0.232	3.00	7.00	535	0.23	⋯	⋯	3.00	70.93	
72	HVS19	173.823958	0.517	−0.980	592.80	96.87	12900	4.53	⋯	⋯	488.21	645.50	Brown et al. (2012)
	3911105521632982400	8.033747	1.079	1.140	11.80	15.17	793	0.29	⋯	⋯	11.80	317.50	
73	HVS20	174.154708	−0.183	−0.990	512.10	75.40	11149	4.21	⋯	⋯	392.39	425.34	Brown et al. (2012)
	3800802102817768832	3.518567	0.656	0.562	8.50	11.11	649	0.28	⋯	⋯	8.50	110.68	
74	HVS22	175.443542	0.065	−0.590	597.80	83.98	11145	4.35	⋯	⋯	484.57	504.51	Brown et al. (2014)
	3897063727354575488	4.704803	0.875	0.674	13.40	13.54	859	0.30	⋯	⋯	13.40	139.37	
75	HVS10	180.907700	−1.086	−0.991	467.90	51.76	11270	4.38	⋯	⋯	413.70	439.40	Brown et al. (2007)
	3926757653770374272	18.047330	0.451	0.207	5.60	5.72	533	0.23	⋯	⋯	5.60	36.45	

Table A1
(Continued)

ID	Notation Gaia ID	R.A. Decl. (deg)	$\mu_\alpha \cos\delta$ $\sigma_{\mu_\alpha \cos\delta}$ (mas yr^{-1})	μ_δ σ_{μ_δ} (mas yr^{-1})	$v_{\rm los}$ $\sigma_{v_{\rm los}}$ (km s^{-1})	d σ_d (kpc)	$T_{\rm eff}$ $\sigma_{T_{\rm eff}}$ (K)	$\log g$ $\sigma_{\log g}$ (dex)	[Fe/H] $\sigma_{\rm [Fe/H]}$ (dex)	[α/Fe] $\sigma_{\rm [\alpha/Fe]}$ (dex)	$V_{\rm rf}$ $\sigma_{V_{\rm rf}}$ (km s^{-1})	$V_{\rm GSR}$ $\sigma_{V_{\rm GSR}}$ (km s^{-1})	Reference
76	HIP 60350	185.623360	−13.304	15.033	262.00	3.10	16100	4.10	⋯	⋯	302.95	532.43	Irrgang et al. (2010)
	1533367925276710272	40.826545	0.041	0.047	5.00	0.60	500	0.15	⋯	⋯	5.00	39.86	
77	HVS16	186.347500	−1.290	−0.535	429.80	65.00	10388	3.96	⋯	⋯	341.81	434.07	Brown et al. (2009)
	3708104343359742848	5.376056	0.501	0.294	7.00	6.00	666	0.29	⋯	⋯	7.00	97.26	
78	LP40-365	211.647710	−49.569	148.642	498.00	0.30	⋯	⋯	⋯	⋯	667.58	737.40	Vennes et al. (2017)
	1711956376295435520	74.316110	0.029	0.029	1.10	0.11	⋯	⋯	⋯	⋯	1.10	28.72	
79	HVS23	240.537580	⋯	⋯	259.30	114.87	10996	3.99	⋯	⋯	307.14	⋯	Brown et al. (2014)
	⋯	0.912272	⋯	⋯	9.80	20.10	778	0.29	⋯	⋯	9.80	⋯	
80	J1603-6613	240.766917	39.872	−7.176	−485.00	1.77	10590	5.34	⋯	⋯	−637.99	811.01	Raddi et al. (2019)
	5822236741381879040	−66.224139	0.048	0.076	5.00	0.34	370	0.20	⋯	⋯	5.00	38.24	
81	LAMOST-HVS2	245.086520	−2.398	−0.803	341.00	22.24	20600	⋯	⋯	⋯	501.31	510.77	Huang et al. (2017)
	1330715287893559936	37.794456	0.027	0.033	7.79	4.57	⋯	⋯	⋯	⋯	7.79	10.93	
82	D6-1	249.381980	−80.232	−195.960	1200.00	1.87	⋯	⋯	⋯	⋯	1038.44	2001.47	Shen et al. (2018)
	5805243926609660032	−74.343490	0.060	0.064	40.00	0.25	⋯	⋯	⋯	⋯	40.00	219.52	
83	HVS17	250.484958	−1.129	−0.930	250.20	49.59	12350	3.80	⋯	⋯	437.00	474.02	Brown et al. (2012)
	1407293627068696192	47.396140	0.090	0.096	2.90	4.34	290	0.09	⋯	⋯	2.90	14.37	
84	D6-3	283.007850	9.406	211.788	−20.00	2.52	⋯	⋯	⋯	⋯	212.53	2510.79	Shen et al. (2018)
	2156908318076164224	62.036168	0.136	0.149	80.00	0.65	⋯	⋯	⋯	⋯	80.00	660.07	
85	D6-2	324.612490	98.285	240.182	20.00	0.83	⋯	⋯	⋯	⋯	250.98	1127.32	Shen et al. (2018)
	1798008584396457088	25.373712	0.068	0.058	60.00	0.04	⋯	⋯	⋯	⋯	60.00	52.77	
86	S5-HVS1	343.715345	35.406	0.535	1017.00	8.88	9630	4.23	0.29	⋯	964.19	1727.36	Koposov et al. (2020)
	6513109241989477504	−51.195610	0.029	0.038	2.70	0.01	110	0.03	0.08	⋯	2.70	2.32	
87	LAMOST-HVS4	344.656500	0.133	−0.338	359.00	27.90	15140	3.90	0.29	⋯	592.12	595.77	Li et al. (2018)
	1928660566125735680	40.001470	0.057	0.063	7.00	1.50	578	0.30	0.18	⋯	7.00	7.06	
88	HVS18	352.270583	0.007	−0.239	237.30	77.70	11993	4.08	⋯	⋯	452.39	463.23	Brown et al. (2012)
	2872564390598678016	33.003186	0.337	0.316	6.40	11.09	516	0.22	⋯	⋯	6.40	33.84	

Notes.
[a] This candidate is also reported by Li21.
[b] This candidate is also reported by Bromley et al. (2018) and Li21.

(This table is available in machine-readable form.)

ORCID iDs

Yang Huang https://orcid.org/0000-0003-3250-2876
Xiao-Bo Dong https://orcid.org/0000-0002-2449-9550
Hua-Wei Zhang https://orcid.org/0000-0002-7727-1699
Timothy C. Beers https://orcid.org/0000-0003-4573-6233
Zhen Yuan https://orcid.org/0000-0002-8129-5415

References

Abadi, M. G., Navarro, J. F., & Steinmetz, M. 2009, ApJL, 691, L63
Adelman-McCarthy, J. K., Agüeros, M. A., Allam, S. S., et al. 2008, ApJS, 175, 297
Ahumada, R., Prieto, C. A., Almeida, A., et al. 2020, ApJS, 249, 3
Alam, S., Albareti, F. D., Allende Prieto, C., et al. 2015, ApJS, 219, 12
Allende Prieto, C., Sivarani, T., Beers, T. C., et al. 2008, AJ, 136, 2070
Anguiano, B., Majewski, S. R., Hayes, C. R., et al. 2020, AJ, 160, 43
Bailer-Jones, C. A. L. 2015, PASP, 127, 994
Bauer, E. B., White, C. J., & Bildsten, L. 2019, ApJ, 887, 68
Baumgardt, H., & Vasiliev, E. 2021, MNRAS, 505, 5957
Bhat, A., Irrgang, A., & Heber, U. 2022, A&A, 663, A39
Blaauw, A. 1961, Bull. Astron. Inst.Netherlands, 15, 265
Bland-Hawthorn, J., & Gerhard, O. 2016, ARA&A, 54, 529
Boubert, D., & Evans, N. W. 2016, ApJL, 825, L6
Boubert, D., Guillochon, J., Hawkins, K., et al. 2018, MNRAS, 479, 2789
Boubert, D., Strader, J., Aguado, D., et al. 2019, MNRAS, 486, 2618
Bovy, J. 2015, ApJS, 216, 29
Bovy, J., Allende Prieto, C., Beers, T. C., et al. 2012, ApJ, 759, 131
Bressan, A., Marigo, P., Girardi, L., et al. 2012, MNRAS, 427, 127
Bromley, B. C., Kenyon, S. J., Brown, W. R., & Geller, M. J. 2018, ApJ, 868, 25
Brown, W. R., Geller, M. J., & Kenyon, S. J. 2009, ApJ, 690, 1639
Brown, W. R., Geller, M. J., & Kenyon, S. J. 2012, ApJ, 751, 55
Brown, W. R., Geller, M. J., & Kenyon, S. J. 2014, ApJ, 787, 89
Brown, W. R., Geller, M. J., Kenyon, S. J., & Kurtz, M. J. 2005, ApJL, 622, L33
Brown, W. R., Geller, M. J., Kenyon, S. J., & Kurtz, M. J. 2006, ApJ, 647, 303
Brown, W. R., Geller, M. J., Kenyon, S. J., Kurtz, M. J., & Bromley, B. C. 2007, ApJ, 671, 1708
Buder, S., Asplund, M., Duong, L., et al. 2018, MNRAS, 478, 4513
Carollo, D., Beers, T. C., Chiba, M., et al. 2010, ApJ, 712, 692
Carretta, E., Bragaglia, A., Gratton, R. G., et al. 2010, A&A, 520, A95
Carretta, E., Bragaglia, A., Gratton, R. G., et al. 2014, A&A, 561, A87
Contigiani, O., Rossi, E. M., & Marchetti, T. 2019, MNRAS, 487, 4025
Cui, X.-Q., Zhao, Y.-H., Chu, Y.-Q., et al. 2012, RAA, 12, 1197
Dawson, K. S., Schlegel, D. J., Ahn, C. P., et al. 2013, AJ, 145, 10
De Silva, G. M., Freeman, K. C., Bland-Hawthorn, J., et al. 2015, MNRAS, 449, 2604
Deason, A. J., Fattahi, A., Belokurov, V., et al. 2019, MNRAS, 485, 3514
Deng, L.-C., Newberg, H. J., Liu, C., et al. 2012, RAA, 12, 735
Dias, W. S., Monteiro, H., Moitinho, A., et al. 2021, MNRAS, 504, 356
Drake, A. J., Catelan, M., Djorgovski, S. G., et al. 2013a, ApJ, 765, 154
Drake, A. J., Catelan, M., Djorgovski, S. G., et al. 2013b, ApJ, 763, 32
Drake, A. J., Djorgovski, S. G., Catelan, M., et al. 2017, MNRAS, 469, 3688
Drake, A. J., Graham, M. J., Djorgovski, S. G., et al. 2014, ApJS, 213, 9
Du, C., Li, H., Newberg, H. J., et al. 2018, ApJL, 869, L31
Du, C., Li, H., Yan, Y., et al. 2019, ApJS, 244, 4
Edelmann, H., Napiwotzki, R., Heber, U., Christlieb, N., & Reimers, D. 2005, ApJL, 634, L181
Eilers, A.-C., Hogg, D. W., Rix, H.-W., & Ness, M. K. 2019, ApJ, 871, 120
Erkal, D., Boubert, D., Gualandris, A., Evans, N. W., & Antonini, F. 2019, MNRAS, 483, 2007
Fragione, G., & Gualandris, A. 2019, MNRAS, 489, 4543
Fritz, T. K., Battaglia, G., Pawlowski, M. S., et al. 2018, A&A, 619, A103
Gaia Collaboration, Brown, A. G. A., Vallenari, A., et al. 2018, A&A, 616, A1
Gaia Collaboration, Brown, A. G. A., Vallenari, A., et al. 2021, A&A, 649, A1
Gaia Collaboration, Eyer, L., Rimoldini, L., et al. 2019, A&A, 623, A110
Gaia Collaboration, Prusti, T., de Bruijne, J. H. J., et al. 2016, A&A, 595, A1
GRAVITY Collaboration, Abuter, R., Amorim, A., et al. 2019, A&A, 625, L10
Geier, S., Fürst, F., Ziegerer, E., et al. 2015, Sci, 347, 1126
Generozov, A., & Perets, H. B. 2022, MNRAS, 513, 4257
Gentile Fusillo, N. P., Tremblay, P.-E., Gänsicke, B. T., et al. 2019, MNRAS, 482, 4570
Gnedin, O. Y., Gould, A., Miralda-Escudé, J., & Zentner, A. R. 2005, ApJ, 634, 344
Gualandris, A., & Merritt, D. 2009, ApJ, 705, 361
Gvaramadze, V. V., Gualandris, A., & Portegies Zwart, S. 2009, MNRAS, 396, 570
Han, Z. 2008, ApJL, 677, L109
Hansen, B. M. S. 2003, ApJ, 582, 915
Harris, W. E. 2010, arXiv:1012.3224
Hattori, K., Valluri, M., Bell, E. F., & Roederer, I. U. 2018, ApJ, 866, 121
Hattori, K., Valluri, M., Castro, N., et al. 2019, ApJ, 873, 116
Heber, U., Edelmann, H., Napiwotzki, R., Altmann, M., & Scholz, R. D. 2008, A&A, 483, L21
Helmi, A., White, S. D. M., de Zeeuw, P. T., & Zhao, H. 1999, Natur, 402, 53
Hills, J. G. 1988, Natur, 331, 687
Hirsch, H. A., Heber, U., O'Toole, S. J., & Bresolin, F. 2005, A&A, 444, L61
Huang, Y., Li, Q., Zhang, H., et al. 2021, ApJL, 907, L42
Huang, Y., Liu, X. W., Chen, B. Q., et al. 2018, AJ, 156, 90
Huang, Y., Liu, X. W., Yuan, H. B., et al. 2015, MNRAS, 449, 162
Huang, Y., Liu, X. W., Yuan, H. B., et al. 2016, MNRAS, 463, 2623
Huang, Y., Liu, X. W., Zhang, H. W., et al. 2017, ApJL, 847, L9
Irrgang, A., Dimpel, M., Heber, U., & Raddi, R. 2021, A&A, 646, L4
Irrgang, A., Geier, S., Heber, U., Kupfer, T., & Fürst, F. 2019, A&A, 628, L5
Irrgang, A., Kreuzer, S., & Heber, U. 2018, A&A, 620, A48
Irrgang, A., Przybilla, N., Heber, U., Nieva, M. F., & Schuh, S. 2010, ApJ, 711, 138
Jayasinghe, T., Kochanek, C. S., Stanek, K. Z., et al. 2018, MNRAS, 477, 3145
Jayasinghe, T., Stanek, K. Z., Kochanek, C. S., et al. 2019a, MNRAS, 486, 1907
Jayasinghe, T., Stanek, K. Z., Kochanek, C. S., et al. 2019b, MNRAS, 485, 961
Jönsson, H., Holtzman, J. A., Allende Prieto, C., et al. 2020, AJ, 160, 120
Jurić, M., Ivezić, Ž., Brooks, A., et al. 2008, ApJ, 673, 864
Justham, S., Wolf, C., Podsiadlowski, P., & Han, Z. 2009, A&A, 493, 1081
Katz, D., Sartoretti, P., Guerrier, A., et al. 2022, arXiv:2206.05902
Kirby, E. N., Cohen, J. G., Smith, G. H., et al. 2011, ApJ, 727, 79
Koposov, S. E., Boubert, D., Li, T. S., et al. 2020, MNRAS, 491, 2465
Koppelman, H. H., Helmi, A., Massari, D., Price-Whelan, A. M., & Starkenburg, T. K. 2019, A&A, 631, L9
Kreuzer, S., Irrgang, A., & Heber, U. 2020, A&A, 637, A53
Kunder, A., Kordopatis, G., Steinmetz, M., et al. 2017, AJ, 153, 75
Lee, Y. S., Beers, T. C., Allende Prieto, C., et al. 2011, AJ, 141, 90
Lee, Y. S., Beers, T. C., Sivarani, T., et al. 2008a, AJ, 136, 2022
Lee, Y. S., Beers, T. C., Sivarani, T., et al. 2008b, AJ, 136, 2050
Leonard, P. J. T. 1991, AJ, 101, 562
Leonard, P. J. T., & Duncan, M. J. 1990, AJ, 99, 608
Li, H., Du, C., Ma, J., et al. 2022, ApJ, 933, 13
Li, J., Jia, S., Gao, Y., et al. 2020, RAA, 20, 042
Li, Y., Luo, A., Zhao, G., et al. 2012, ApJL, 744, L24
Li, Y.-B., Luo, A. L., Lu, Y.-J., et al. 2021, ApJS, 252, 3
Li, Y.-B., Luo, A. L., Zhao, G., et al. 2015, RAA, 15, 1364
Li, Y.-B., Luo, A. L., Zhao, G., et al. 2018, AJ, 156, 87
Liao, J., Du, C., Li, H., Ma, J., & Shi, J. 2023, ApJL, 944, L39
Lindegren, L., Bastian, U., Biermann, M., et al. 2021, A&A, 649, A4
Lindegren, L., Hernández, J., Bombrun, A., et al. 2018, A&A, 616, A2
Liu, X. W., Yuan, H. B., Huo, Z. Y., et al. 2014, in Setting the Scene for Gaia and LAMOST, ed. S. Feltzing et al., Vol. 298 (Cambridge: Cambridge Univ. Press), 310
Luo, A. L., Zhao, Y.-H., Zhao, G., et al. 2015, RAA, 15, 1095
Majewski, S. R., Schiavon, R. P., Frinchaboy, P. M., et al. 2017, AJ, 154, 94
Marchetti, T. 2021, MNRAS, 503, 1374
Marchetti, T., Evans, F. A., & Rossi, E. M. 2022, MNRAS, 515, 767
Marchetti, T., Rossi, E. M., & Brown, A. G. A. 2019, MNRAS, 490, 157
Marigo, P., Girardi, L., Bressan, A., et al. 2017, ApJ, 835, 77
McConnachie, A. W. 2012, AJ, 144, 4
McMillan, P. J. 2018, RNAAS, 2, 51
Monari, G., Famaey, B., Carrillo, I., et al. 2018, A&A, 616, L9
Mottini, M., Wallerstein, G., & McWilliam, A. 2008, AJ, 136, 614
Naidu, R. P., Conroy, C., Bonaca, A., et al. 2020, ApJ, 901, 48
Neunteufel, P. 2020, A&A, 641, A52
Pakmor, R., Kromer, M., Taubenberger, S., & Springel, V. 2013, ApJL, 770, L8
Palladino, L. E., Schlesinger, K. J., Holley-Bockelmann, K., et al. 2014, ApJ, 780, 7
Patel, E., Kallivayalil, N., Garavito-Camargo, N., et al. 2020, ApJ, 893, 121
Piffl, T., Williams, M., & Steinmetz, M. 2011, A&A, 535, A70
Portegies Zwart, S. F. 2000, ApJ, 544, 437
Poveda, A., Ruiz, J., & Allen, C. 1967, BOTT, 4, 86
Price-Whelan, A., Sipocz, B., Major, S., & Oh, S. 2017, adrn/gala: v0.2.1, Zenodo, doi:10.5281/zenodo.833339

Prudil, Z., Koch-Hansen, A. J., Lemasle, B., et al. 2022, A&A, 664, A148
Przybilla, N., Fernanda Nieva, M., Heber, U., & Butler, K. 2008, ApJL, 684, L103
Quispe-Huaynasi, F., Roig, F., McDonald, D. J., et al. 2022, AJ, 164, 187
Raddi, R., Hollands, M. A., Gänsicke, B. T., et al. 2018, MNRAS, 479, L96
Raddi, R., Hollands, M. A., Koester, D., et al. 2019, MNRAS, 489, 1489
Rasskazov, A., Fragione, G., Leigh, N. W. C., et al. 2019, ApJ, 878, 17
Reggiani, H., Ji, A. P., Schlaufman, K. C., et al. 2022, AJ, 163, 252
Reid, M. J., & Brunthaler, A. 2004, ApJ, 616, 872
Reid, M. J., Menten, K. M., Brunthaler, A., et al. 2014, ApJ, 783, 130
Rockosi, C. M., Lee, Y. S., Morrison, H. L., et al. 2022, ApJS, 259, 60
Rossi, E. M., Marchetti, T., Cacciato, M., Kuiack, M., & Sari, R. 2017, MNRAS, 467, 1844
Samus', N. N., Kazarovets, E. V., Durlevich, O. V., Kireeva, N. N., & Pastukhova, E. N. 2017, ARep, 61, 80
Sbordone, L., Bonifacio, P., Marconi, G., Buonanno, R., & Zaggia, S. 2005, A&A, 437, 905
Schönrich, R. 2012, MNRAS, 427, 274
Schönrich, R., McMillan, P., & Eyer, L. 2019, MNRAS, 487, 3568
Seabroke, G. M., Fabricius, C., Teyssier, D., et al. 2021, A&A, 653, A160
Shappee, B. J., Prieto, J. L., Grupe, D., et al. 2014, ApJ, 788, 48
Shen, K. J., Boubert, D., Gänsicke, B. T., et al. 2018, ApJ, 865, 15
Siegert, T. 2019, A&A, 632, L1
Smolinski, J. P., Lee, Y. S., Beers, T. C., et al. 2011, AJ, 141, 89
Steinmetz, M., Zwitter, T., Siebert, A., et al. 2006, AJ, 132, 1645
Taylor, M. B. 2005, in ASP Conf. Ser. 347, Astronomical Data Analysis Software and Systems XIV, ed. P. Shopbell, M. Britton, & R. Ebert (San Francisco, CA: ASP), 29
Tillich, A., Przybilla, N., Scholz, R. D., & Heber, U. 2009, A&A, 507, L37
Tolstoy, E., Hill, V., & Tosi, M. 2009, ARA&A, 47, 371
Torrealba, G., Catelan, M., Drake, A. J., et al. 2015, MNRAS, 446, 2251
Vasiliev, E. 2019, MNRAS, 484, 2832
Vasiliev, E., & Baumgardt, H. 2021, MNRAS, 505, 5978
Venn, K. A., Irwin, M., Shetrone, M. D., et al. 2004, AJ, 128, 1177
Vennes, S., Nemeth, P., Kawka, A., et al. 2017, Sci, 357, 680
Wang, B., & Han, Z. 2009, A&A, 508, L27
Williams, A. A., Belokurov, V., Casey, A. R., & Evans, N. W. 2017, MNRAS, 468, 2359
Xiang, M., Ting, Y.-S., Rix, H.-W., et al. 2019, ApJS, 245, 34
Xue, X. X., Rix, H. W., Zhao, G., et al. 2008, ApJ, 684, 1143
Yanny, B., Rockosi, C., Newberg, H. J., et al. 2009, AJ, 137, 4377
Yu, Q., & Tremaine, S. 2003, ApJ, 599, 1129
Zhao, G., Zhao, Y., Chu, Y., Jing, Y., & Deng, L. 2012, RAA, 12, 732
Zheng, Z., Carlin, J. L., Beers, T. C., et al. 2014, ApJL, 785, L23
Zhou, Y., Li, X., Huang, Y., & Zhang, H. 2022, ApJ, 946, 73
Ziegerer, E., Volkert, M., Heber, U., et al. 2015, A&A, 576, L14
Zinn, J. C., Pinsonneault, M. H., Huber, D., & Stello, D. 2019, ApJ, 878, 136
Zubovas, K., Wynn, G. A., & Gualandris, A. 2013, ApJ, 771, 118